J. Fluid Mech. (2002), *vol.* 469, *pp.* 89–120.
DOI: 10.1017/S0022112002001684 Printed in the United Kingdom

Free-surface turbulent wake behind towed ship models: experimental measurements, stability analyses and direct numerical simulations

By LIAN SHEN, CHIONG ZHANG† AND DICK K. P. YUE

Department of Ocean Engineering, Massachusetts Institute of Technology, Cambridge, MA 02139, USA

(Received 16 August 2001 and in revised form 25 April 2002)

We combine experimental, theoretical and numerical efforts to investigate the turbulent wake far behind a surface ship at model scales. Experimental measurements using digital particle image velocimetry (DPIV) are performed for the wakes of three towed hulls with beam-to-draught ratios $b/d = 1, 2, 6$. Based on model speed and beam, the Reynolds and Froude numbers are $O(10^3)$ and $O(10^{-2})$ respectively. Distinct surface features associated with persistent surface-normal vorticity have been identified, which are characterized by large-scale meandering structures. Both lateral and longitudinal scales of the meandering are quantified, with the former found to increase as b/d decreases and the latter independent of b/d. Based on measurements at multiple horizontal and vertical planes, profiles of the mean flow and fluctuation intensity for each velocity component are obtained. To understand the turbulence transition mechanism, an Orr–Sommerfeld stability analysis (OS) is formulated for the wake flow with free-surface boundary conditions, and solved by using a fourth-order finite-difference scheme. Unstable modes antisymmetric to the wake centre-plane are identified. Consistent with the experimental results, the growth rates of unstable modes increase substantially as b/d decreases, while the dependence of meandering wavelengths on b/d is found to be weak. Finally, we perform direct numerical simulation (DNS) of Navier–Stokes equations for the wake flow. The growth rates of unstable modes agree well with the predictions by OS analysis. Compared with experiments, DNS accurately captures the surface-normal vorticity signatures, the meandering features, as well as statistics of turbulence intensity. We also obtain from DNS a detailed description of enstrophy, turbulence length scales, and vortex structures for the wake flow.

1. Introduction

Ship wake flows have been of interest in fluid mechanics for a long time. In the past, the classical Kelvin wave pattern has received most attention and has been extensively investigated. Recently, however, the turbulent wakes behind ships have attracted special interest, largely due to the need to interpret the radar observations of ship wakes (cf. Munk, Scully-Power & Zachariasen 1987; Sarpkaya 1996). Synthetic Aperture Radar images reveal the existence of a narrow V-like wake, with a half-angle typically between 2° and 3°, which extends some 20 km behind a surface ship. This observation does not belong to the Kelvin wake pattern and is believed to

† Present address: Schlumberger, Austin Product Center, Austin, TX, USA.

be related to short-wave-damping phenomena involving free-surface turbulent flows, surface-active materials, and the redistribution of surface impurities by currents and bubbles.

Our ability to interpret phenomena such as the observed narrow V-shaped ship wakes is much constrained by limited understanding of the relevant fluid mechanics of the turbulent flow in the wake and its interactions with the free surface. The study of free-surface turbulence (FST) is an arduous task. In addition to the usual complexity of turbulence study, it also possesses additional difficulties such as the complex geometry of a deformable free surface, the highly nonlinear wave–turbulence interaction, the effects of surface vorticity, and surfactant dynamics.

In this paper we perform a mechanistic study of turbulent free-surface wake flows behind a towed ship model. Our object is to reveal the fundamental physics rather than the engineering applications. As a first step towards the understanding of the turbulent wake, we restrict our attention to simple ship hull geometries at model scales with corresponding Reynolds and Froude numbers low enough such that accurate whole-field laboratory measurements and (direct) numerical simulations can be performed. To provide a comprehensive picture and to cross-validate the predictions we make, we employ a coordinated effort using quantitative whole-field measurement, Orr–Sommerfeld stability analysis, and direct numerical simulation for the same geometry and at the same Reynolds and Froude scales.

For a long time, traditional experimental studies of turbulent flow had perforce relied upon flow visualization for flow structure information and had used conditional sampling methods to obtain flow statistics information. A significant achievement of modern experimental fluid mechanics is the invention and development of techniques for the quantitative measurement of the whole, instantaneous flow field (Adrian 1991). The digital particle image velocimetry (DPIV) technique makes it possible to measure a large number of simultaneous velocity components in a two-dimensional region of the fluid flow. This has proven to be a powerful tool for FST research (see e.g. Gharib, Dabiri & Zhang 1994). In this work, we use DPIV to perform quantitative whole-field measurements of free-surface turbulent wakes on multiple horizontal and vertical planes. These allow us to identify the general features of the wake, and to provide the initial conditions and data for direct quantitative comparisons at later times for the subsequent theoretical stability analyses and numerical simulations.

The Orr–Sommerfeld (OS) stability analysis is another powerful tool in the study of free-surface turbulent wakes. The linear stability analysis clarifies some of the mechanisms by which turbulence is generated and maintained. Although the processes in the fully developed turbulence, where the nonlinearity plays an essential role, are much more complicated than the linear instability processes, the latter nevertheless give important insights into the fluctuations which may arise in a flow. For example, Triantafyllou & Dimas (1989) have shown that the existence of a free surface drastically alters the turbulence transition properties of a two-dimensional shear flow. In this study we formulate and solve the Orr–Sommerfeld equations for the three-dimensional wake flow subject to the free-surface boundary conditions. As will be shown, the stability analysis facilitates the explanation of experimental observations, the construction of initial conditions for numerical simulations, and the cross-validation between the two.

Finally, we employ direct numerical simulation (DNS) in this study of the free-surface turbulent wake. With the rapid growth in both the size and speed of computers, numerical simulation has become an indispensable tool in turbulence research. A number of DNS have been performed for free-surface turbulent flows: Lam

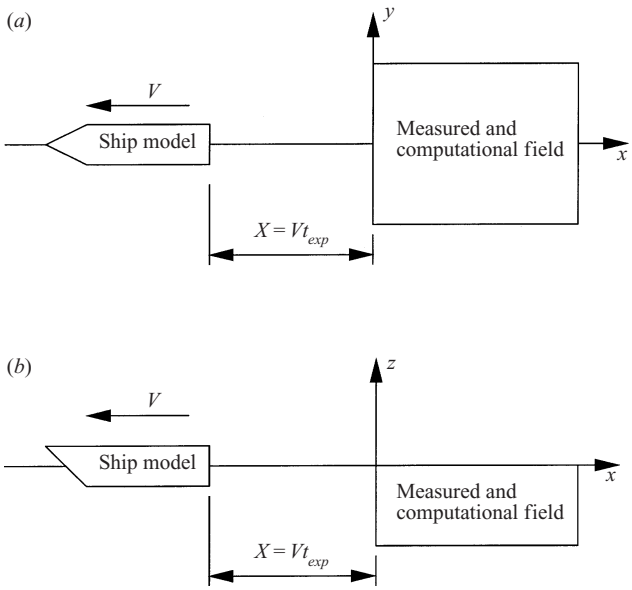

FIGURE 1. Schematic of the free-surface turbulent wake field behind a towed ship model: (*a*) top view and (*b*) side view.

& Banerjee (1988), Handler *et al.* (1993), Komori *et al.* (1993), Borue, Orszag & Staroselsky (1995), Perot & Moin (1995), Walker, Leighton & Garza-Rios (1996) and Shen, Triantafyllou & Yue (1999), to cite a few. Numerical simulation has the advantage of providing whole-field (spatial and temporal) data for all the physical quantities computed. Once robust numerical capability is established, substantial information on the statistical, structural and dynamical properties of the flow field can be obtained.

In the present paper we combine experimental (DPIV), theoretical (OS), and numerical (DNS) approaches to investigate the turbulent wake behind towed ship models. For this coordinated research effort, the key objective is to obtain direct quantitative comparison and cross-validation among the approaches. The outline of the paper is as follows. We define the physical problem in § 2. In § 3, we use DPIV to obtain the wake features and identify the meandering of surface-connected vortices as a key feature of such wakes. We also obtain from these measurements the wake profiles which are a basis for the later theoretical and numerical analyses. In § 4, we perform an Orr–Sommerfeld stability analysis on the mean wake profile and obtain results which help to explain the observed meandering phenomena. In § 5, DNS are performed and the results are compared satisfactorily to the experimental and theoretical findings. Finally in § 6, we present our conclusions.

2. Problem definition

We investigate the far wake field behind a towed ship model. We choose a reference frame fixed in space with the tank (figure 1). The model travels in the negative x-direction with a speed V; the y-axis points in the beamwise direction and the z-axis is positive upward. The origin is located at the undisturbed free surface and $y = 0$ is the ship symmetry plane. For definiteness, the time $t_{exp} = 0$ is defined as the instant the ship stern passes the origin.

	Length L (cm)	Beam b (cm)	Draught d (cm)	Beam-to-draught ratios b/d
Hull I	50	4.0	0.67	6
Hull II	50	4.0	2.0	2
Hull III	50	2.0	2.0	1

TABLE 1. Ship model parameters.

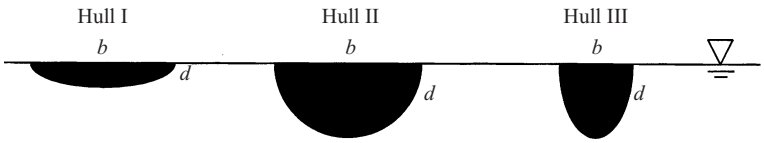

FIGURE 2. Stern cross-section (below the water surface) of ship models.

Our interest is to understand the underlying physics of turbulent wake at these scales and their dependence on basic hull geometric parameters. To do this, we consider three relatively simple ship model geometries (figure 2 and table 1) which have the same length, L, but varying beam-to-draught ratios, b/d. Among these, 'hull II' which has a semi-circular stern cross-section (below the free surface) serves as our base model and for which we present most of the results. The results we present for the other two hulls are primarily to indicate the dependence on b/d. All results are for hull II unless otherwise specified.

The flow examined in this study is non-stationary, and quasi-homogeneous in the streamwise direction. The latter is due to the greater length scale associated with variations in the streamwise direction relative to the transverse directions. We further assume that the statistics are symmetric with respect to the centre-plane $y = 0$, except for specific meandering quantities which we define later (§ 3.2). Thus, at a given time instant, statistical quantities can be obtained by averaging in the streamwise direction at symmetric $(|y|, z)$ positions. In the results presented, for any quantity f, its mean, fluctuation and root-mean-square values are denoted by F, f' and f^{rms}, respectively.

3. Experimental DPIV measurements

3.1. *Experiment setup*

The experimental DPIV measurements of ship model wakes are performed in a tank which measures 240 cm in length, 74 cm across, and 70 cm in depth. It is constructed with glass so that laser light can propagate through it. A towing carriage is located on top of the tank, controlled via a speed adjustment motor. In our experiments, each ship model is mounted at the lateral centre of the tank and special care is exercised to ensure that the models are towed at zero yaw and pitch.

We use fluorescent spheres with diameters of $20 \sim 45\,\mu$m to seed the entire tank for DPIV imaging. An argon-ion laser is employed as the light source. The laser light propagates through a fibre-optic link and cylindrical lens to generate a 2 mm thick laser sheet located on a desired plane. The laser light is controlled by a high-speed mechanical chopper, with the pulse timing signal produced by a General Pixels Video Trigger Generator. A TI MC1134P/GN CCD B/W video camera, which captures the seeded flow images on the ship-wake section, is directed to the EPIX 4MEG VIDEO Framer Grabber and the Video Monitor. Finally, we use a SONY CRV

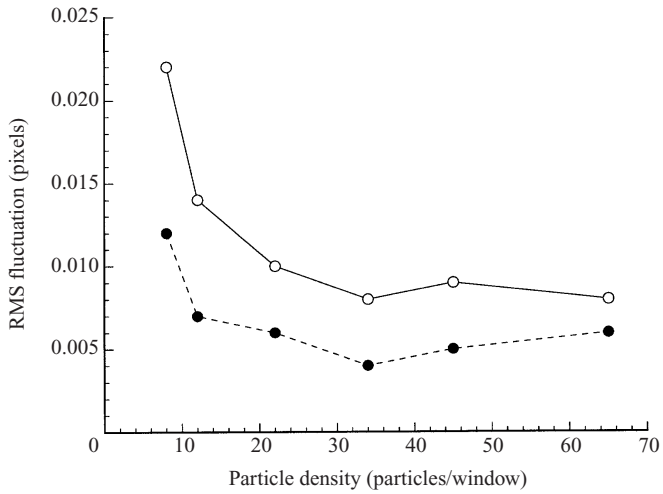

FIGURE 3. Measurement uncertainties of DPIV without spatial shift: horizontal (———) and vertical (- - - - -) fluctuation intensity as a function of particle density.

laserdisc recorder with a resolution of 768×480 pixels and a speed of 30 Hz for the storage and later analysis of flow images. The scaling factor in this experiment is 2.2 pixel mm^{-1} so that the measured wake domain is of size 350 mm $\times$ 220 mm.

For all our analyses of recorded images, we choose a 32×32 pixel-sized window with an 8 pixel stepping. Thus the recorded 768×480 pixel image field is rendered into 96×60 grid points, on which velocity is calculated. In other words, the grid spacing in experimental results is approximately 3.6 mm.

Factors such as the number of particles within the sampling window, the camera and digitizer performance characteristics, and computational errors all affect the final DPIV resolution. In order to estimate the level of accuracy and uncertainty of our measured data, a series of calibration/validation tests have been performed. The details are provided in Zhang (1996). We summarize the main results here.

The calibration tests are performed through random patterns of bright particles captured by our image acquisition system. First, several images are captured with no relative displacement and processed by the DPIV technique. We compile the statistical uncertainty in the measurements in figure 3. It is clear that the uncertainty is a function of the particle density. For the particle density of $20 \sim 30$ particles per window in our ship wake experiments, figure 3 shows that the lowest obtainable uncertainty is approximately 0.01 pixel. Next, we shift image pairs mechanically with respect to each other over all the possible displacements in the 32×32 pixel window. The results are plotted in figure 4. Comparing these results, we find that as the displacements increase, the associated uncertainties increase as well.

Our experimental resolution is obtained from the results shown in figures 3 and 4. For example, if the model speed is 25 mm s^{-1}, the maximum displacement should be $25/30 = 0.83$ mm, or $0.83 \times 2.2 \approx 1.8$ pixels. By checking figure 4, we find that the maximum root-mean-square displacement error is $0.02/2.2 \approx 0.009$ mm, or maximum velocity error is $0.009 \times 30 \approx 0.3$ mm s^{-1}. On the other hand, the minimum displacement can be obtained from figure 3, which is $0.01/2.2 \approx 0.005$ mm. Thus, the minimum detectable velocity is $0.005 \times 30 \approx 0.2$ mm s^{-1}. In this DPIV experiment, the associated dynamic range, the ratio of maximum to minimum measurable displacements, is $0.83/0.005 \approx 170$.

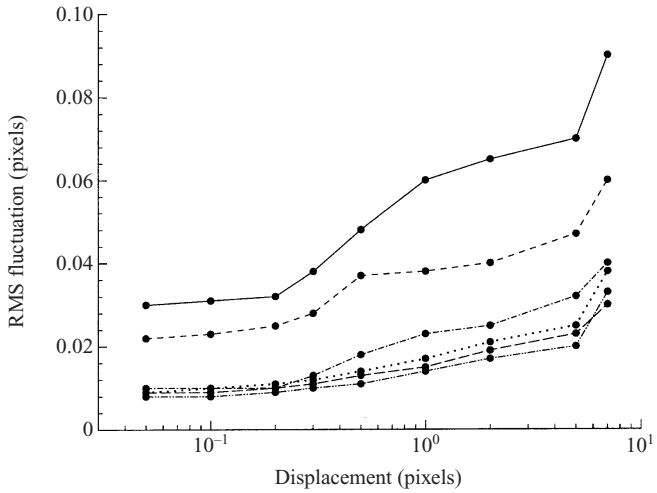

FIGURE 4. Measurement uncertainties of DPIV with spatial shift: fluctuation intensity as a function of displacement for particle densities of 8 (———), 12 (- - - - -), 22 (– · – · –), 34 (· · · · · · ·), 45 (— —) and 65 (—··—··—) particles per window.

Finally we note that the surfactants which exist on the free surface may in some way affect our velocity measurements near the free surface. To remove these effects, we inject some dish detergent on the free surface and sweep the surfactants to a drain located at one end of the tank which has the same level as the water level in the tank. This procedure is repeated frequently between runs.

3.2. *Experiment results*

Due to considerations of the tank dimensions and experimental setup, we select a single towing speed in the experiments corresponding to $V = 25\,\mathrm{mm\,s^{-1}}$. Based on this speed and the model beam, b, the Reynolds and Froude numbers are respectively $Re \equiv Vb/\nu \approx 1000$ and $Fr \equiv V/\sqrt{gb} \approx 0.04$. Here ν is the kinematic viscosity and g is the gravitational acceleration. Hereafter, all the results we present are normalized by V and b.

At each distance X behind the ship model (cf. figure 1), DPIV measurements are performed separately at five horizontal planes ($z/b = -0.05$, -0.13, -0.21, -0.28 and -0.41) and five vertical planes ($y/b = 0$, 0.1, 0.15 0.23 and 0.36). We remark that measurements have also been performed at longitudinal cuts ($x/b =$ const), from which the results are found to be essentially the same as those from $z/b =$ const and $y/b =$ const plane measurements (Zhang 1996) and will not be discussed here. Since our interest is the far wake behind the model, the lower limit of the DPIV measurements is set at $X/b = 5$. Consequently, near-wake phenomena which might be present are not available from these measurements. The upper limit of the measurements corresponds to $X/b = 20$. This is imposed by the dimensions of the tank (tank length $L_0/b = 60$) and the model (length $L/b = 12.5$).

The DPIV technique is able to produce a quantitative description of the instantaneous flow field at a large number of grid points with fine resolution. Figure 5(a) shows a typical example of the results obtained, where the velocity vectors (u, v) at the horizontal plane very close to the free surface ($z/b = -0.05$) are plotted.

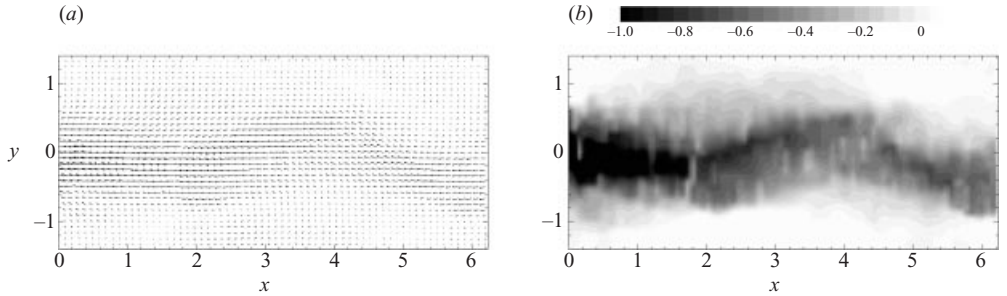

FIGURE 5. DPIV measurements of (a) velocity vector (u,v), and (b) contours of u on the horizontal plane $z/b = -0.05$ at a distance $X/b = 5$ from the ship model.

Based on such plane velocity projections at different locations of the wake, we obtain substantial information on both the statistical and structural aspects of the wake flow.

Meandering feature

A salient feature observed from the DPIV is seen in figure 5, for the instantaneous near-surface ($z/b = -0.05$) horizontal velocity vector field and contours of the longitudinal component u, which shows the meandering nature of the wake. There are two spatial scales associated with the wake meandering: a streamwise scale, L_m, which measures the meandering 'wavelength'; and a lateral scale, A_m, which measures the meandering 'amplitude'. From the figure, we can estimate L_m and A_m to be approximately $4b$ and $0.5b$ respectively (at this depth).

It turns out that this meandering behaviour is one of the most prominent features of the wake. To investigate this in more detail on the free surface, we consider the vertical or surface-normal component of the vorticity ω_z. As shown in Shen *et al.* (1999), for free-surface turbulence, the surface-normal vorticity is highly coherent and persistent and serves as a useful indicator of the underlying dynamics. Figure 6(a) shows the contours of ω_z (calculated using finite differencing of the measured velocity components shown in figure 5a). In figure 5, the measurement is obtained at a plane very close to the free surface ($z/b = -0.05$). As will be shown in § 5, while surface-parallel vorticity components vary dramatically in the vertical direction, the variation of surface-normal vorticity is small. Thus, ω_z at this depth is a close approximation of the connected vortices at the surface. The coherent structures of these vortices are seen in figure 6(a). Because the mean flow is in the negative x-direction and is jet-like with the centre located around the x-axis (cf. figure 1), vorticity in the $y > 0$ half-plane is mostly negative while that in the $y < 0$ half-plane is positive. The meandering of the wake flow is clear.

We next examine the meandering features at different locations of the wake field. Figures 6(b)–6(d) plot ω_z contours at the same near-surface depth but at different downstream distances from the ship model. As the towed model moves away, the lateral meandering amplitude increases and the meandering becomes more prominent. The change in the streamwise meandering wavelength, however, is rather small. Figures 7$(a\mathrm{i})$–7$(e\mathrm{i})$ examine the variation of the meandering at different depths. As the depth increases, the meandering amplitude decreases first and then increases.

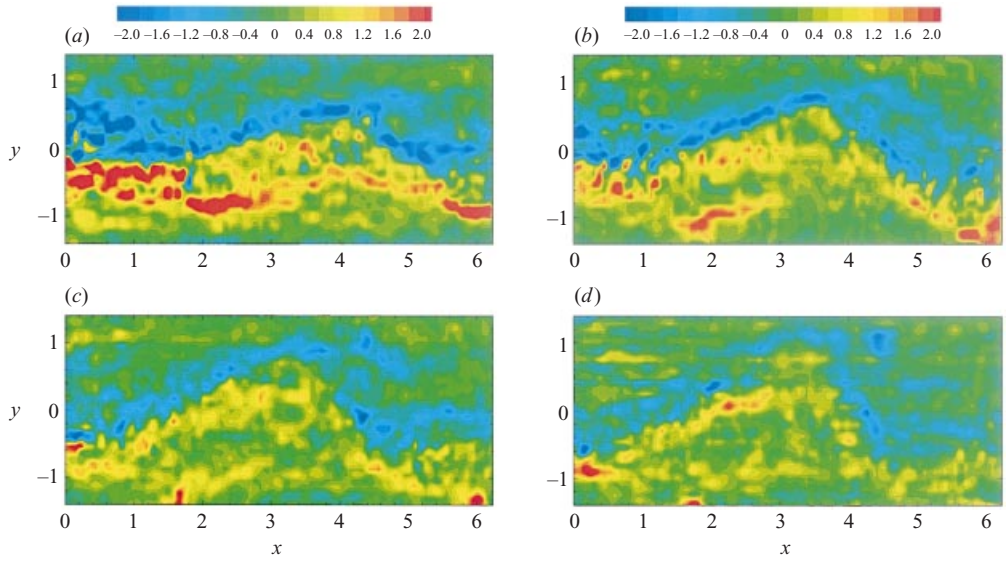

FIGURE 6. DPIV contours of ω_z at the $z/b = -0.05$ plane at distances: (*a*) $X/b = 5$, (*b*) 10, (*c*) 15, and (*d*) 20 from the ship model.

Quantification of meandering scales

To characterize the meandering feature, we provide quantitative definitions for the streamwise wavelength L_m and lateral amplitude A_m of the meandering at a given location based on the vertical vorticity ω_z. We define L_m as the distance over which the streamwise correlation coefficient

$$R_f(\xi) \equiv \frac{\langle f(x)f(x+\xi)\rangle}{\langle f(x)f(x)\rangle} \tag{3.1}$$

attains its (local) maximum value for $f = \omega_z$ at the free surface. In the above equation, $\langle\ \rangle$ denotes averaging over the horizontal DPIV measurement plane.

Figure 8 plots $R_{\omega_z}(\xi)$. As ξ increases, $R_{\omega_z}(\xi)$ decreases (from 1) reaching a minimum around $L_m/2$ and then increases and reaches a local maximum value at $\xi = L_m \approx 4.1b$ (for hull II). This is consistent with the earlier estimate from figure 6 based on velocity contours. The value of $L_m/b \approx 4.1$ corresponds to a Strouhal number $St \equiv b/(V\delta t_{exp}) \approx 0.24$. From DPIV measurements at successive horizontal planes at increasing X/b (figure 6), results similar to figure 8 are obtained (not shown here). From these, we find that the value of this Strouhal number changes little for different X/b.

The lateral amplitude A_m can be defined in terms of the (normalized) vorticity enstrophy moment about the centreline:

$$O(x,z) \equiv \frac{\int_y \omega_z^2 y\,\mathrm{d}y}{\int_y \omega_z^2\,\mathrm{d}y}, \tag{3.2}$$

where the limits of integration in y are the outer edges of the measured field. This enstrophy moment in general contains contributions from both the mean flow and the meandering portion. The contribution due to the mean flow, which we denote as

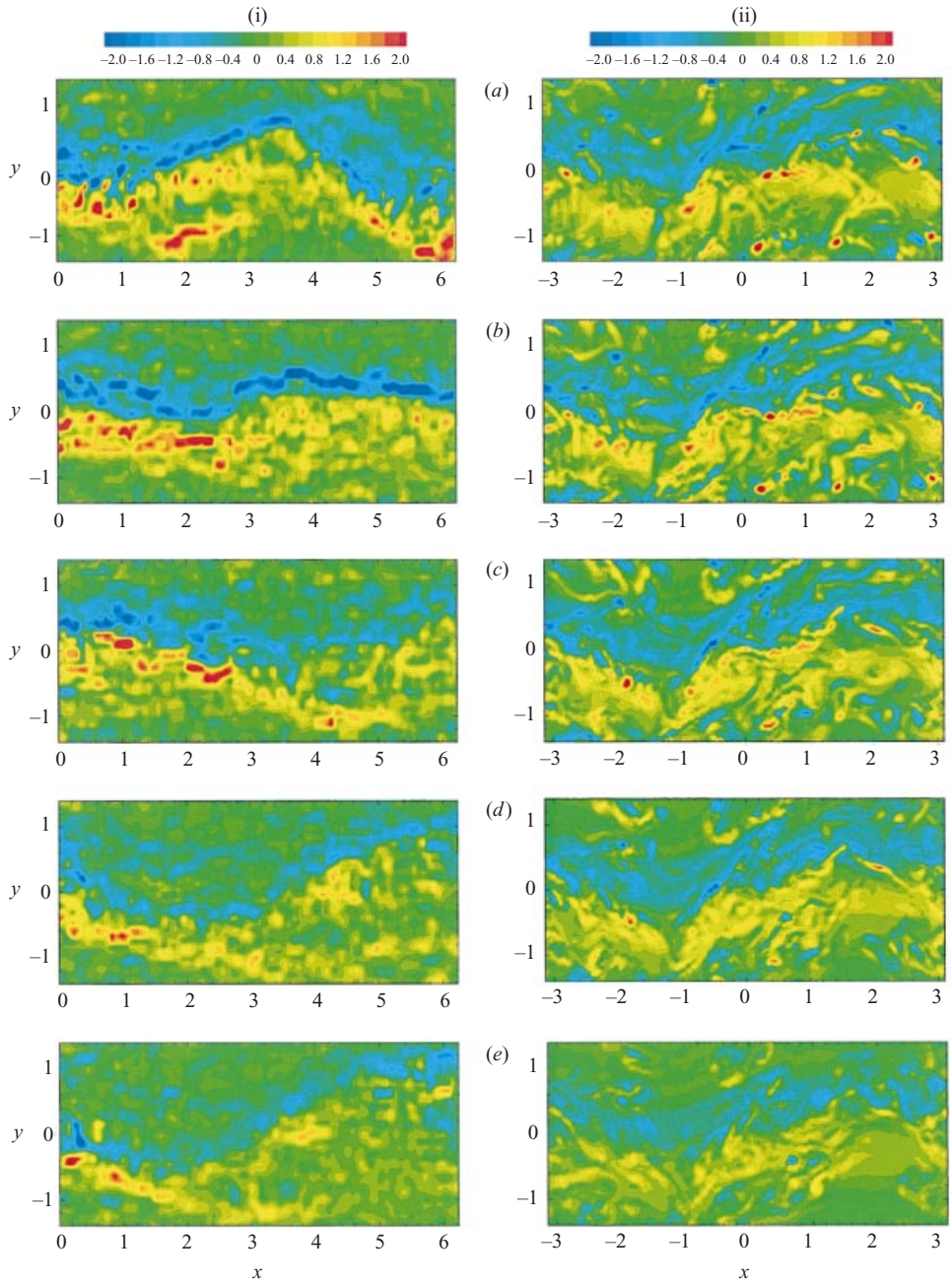

FIGURE 7. Contours of ω_z obtained from (i) DPIV, and (ii) DNS, at planes of depth: (*a*) $z/b = -0.05$, (*b*) -0.13, (*c*) -0.21, (*d*) -0.28, and (*e*) -0.41. In the experiment, the distance from the ship model is $X/b = 10$; in DNS, $t = 15$.

$\overline{O}$, is given by longitudinal averaging (over L_m):

$$\overline{O}(x,z) \equiv \frac{1}{L_m}\int_{-L_m/2}^{L_m/2} O(x+\xi',z)\,\mathrm{d}\xi'. \tag{3.3}$$

Finally, subtracting (3.3) from (3.2), we define the meandering amplitude A_m averaged

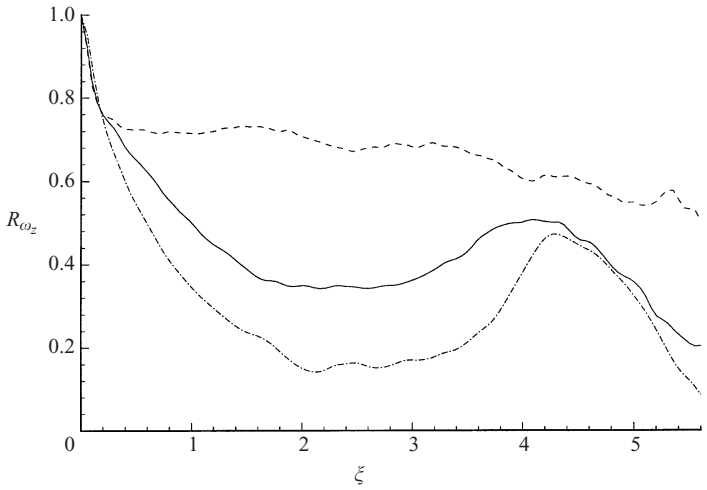

FIGURE 8. Streamwise correlation coefficient $R_{\omega_z}(\xi)$ for: hull I (- - - - -), hull II (———), and hull III (– · – · –). $X/b = 5$ and $z/d = -0.05$.

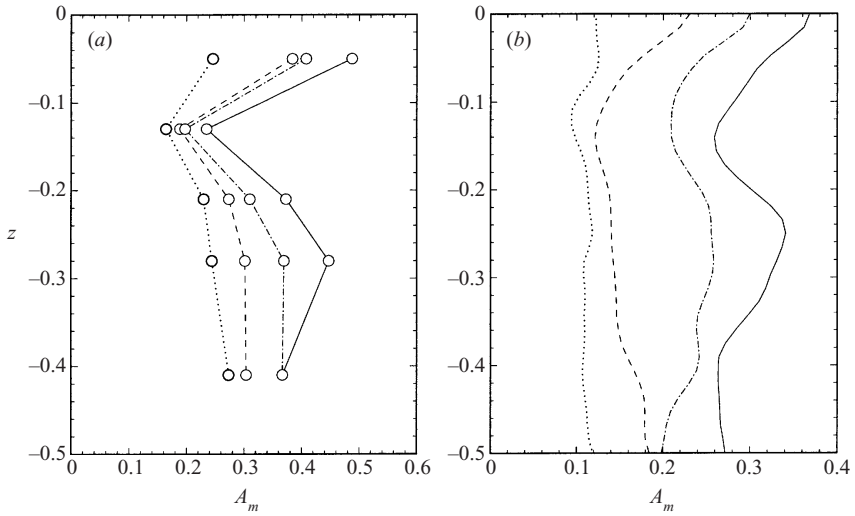

FIGURE 9. Profiles of meandering amplitude A_m obtained from (a) DPIV, and (b) DNS. In the experiment, $X/b =$: 5 (· · · · · · ·), 10 (- - - - -), 15 (– · – · –), and 20 (———); in DNS, $t =$: 5 (· · · · · · ·); 10 (- - - - -); 15 (– · – · –); and 20 (———).

over L_m as

$$A_m(x,z) \equiv \sqrt{\frac{1}{L_m}\int_{-L_m/2}^{L_m/2} (O(x+\xi,z) - skew3\overline{O}(x,z))^2 \,\mathrm{d}\xi}. \tag{3.4}$$

Figure 9(a) plots the profiles of meandering amplitude A_m at different distances from the ship model. It shows that A_m increases with the distance from the ship model, consistent with the earlier observation from figure 6. Figure 9(a) also shows that as the free surface is approached, A_m first decreases and then increases. This is also consistent with the observation from figure 7.

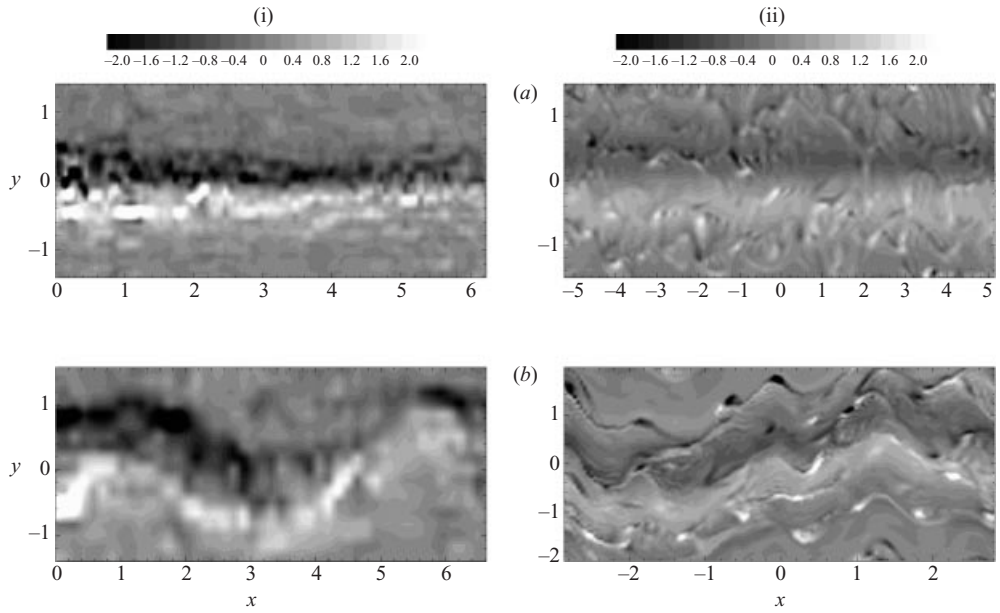

FIGURE 10. Contours of ω_z obtained from (i) DPIV and (ii) DNS, for (*a*) hull I and (*b*) hull III. In DPIV, $z/b = -0.05$ and $X/b = 10$; in DNS, $z/b = 0$ and $t = 15$.

Effects of hull geometry

In order to investigate the effects of hull geometry, we also perform measurements for a shallow hull (hull I, $b/d = 6$) and a deep hull (hull III, $b/d = 1$). Figures 10(*a*i) and 10(*b*i) plot the DPIV ω_z contours for hull I and hull III, respectively. Together with figure 6(*b*) which is for hull II, the geometry effect is shown clearly: the meandering behind the shallow hull is insignificant; the deep hull, on the other hand, produces a much more prominent meandering.

Figure 8 plots the correlation coefficient $R_{\omega_z}(\xi)$ for the different hulls. Unlike hulls II and III, a local maximum is not present in the $R_{\omega_z}(\xi)$ curve for hull I. This is due to the weak meandering feature for hull I (figure 10). On the other hand, $R_{\omega_z}(\xi)$ for hull III shows the sharpest trough and peak of the three hulls, again indicative of the strong features seen in figure 10. Finally, we note that the meandering wavelength L_m is about the same for hulls II and III ($L_m/b \approx 4.1$ and 4.3 respectively).

The effect of the hull beam-to-draught aspect ratio on the meandering feature can be summarized as follows. The prominence of the meandering (both in terms of coherence and lateral amplitude) in general increases as b/d decreases. On the other hand, the meandering (once established) has a wavelength (normalized by b) that is relatively insensitive to b/d. These observations are not unexpected if one thinks of the meandering as instabilities of a mean wake profile of (approximate) aspect ratio b/d. For small b/d, the wake flow qualitatively resembles that behind a (long vertical) cylinder and is expected to be dominated by asymmetric instabilities with a characteristic Strouhal number. As expected, these coherent asymmetric features diminish as b/d increases. This consideration is the basic motivation of the Orr–Sommerfeld stability analysis of the mean free-surface wake flow in § 4.

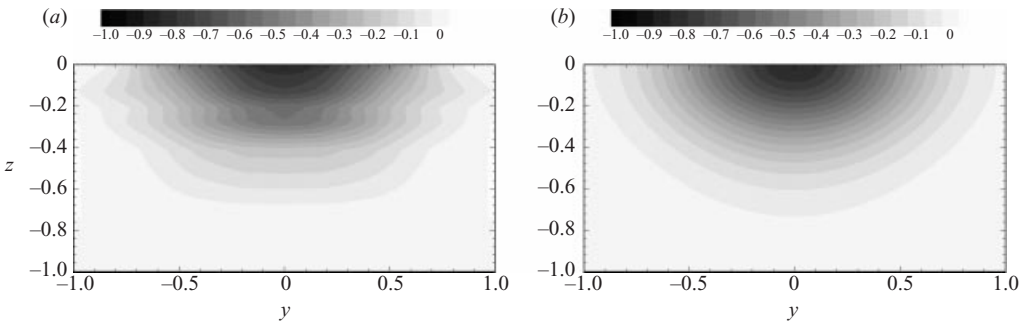

FIGURE 11. Contours of mean velocity $U(y, z)$ obtained from (a) DPIV, and (b) the analytical fitting (4.27). The wake location is $X/b = 10$.

Mean flow velocity and velocity fluctuation intensity profiles

In addition to the turbulent structures elucidated above, the DPIV technique also obtains statistics of the wake field. Measurements at five horizontal planes of different depths provide streamwise and lateral velocity components, while streamwise and vertical velocities are obtained from measurements at vertical planes with five different lateral positions. These together provide a quantitative description of the flow field.

Figure 11(a) plots the mean velocity $U(y, z)$ contours on the (y, z) cross-section. As defined in § 2, averaging is performed in the x-direction. Here and hereafter, the averaging length is set to be the meandering wavelength L_m. For this flow, streamwise variation is much smaller than the variations in the lateral and vertical directions, and the change of U over the streamwise distance L_m is negligible. Not surprisingly, the mean velocity profile has an approximately semi-circular shape with the maximum velocity deficit located at $(y = 0, z = 0)$.

Figures 12(ai)–12(ci) plot the contours of the fluctuation intensity of each velocity component. Fluctuation is defined as the deviation from the mean value (averaging over a meandering wavelength L_m), and its intensity is quantified by the root-mean-square value. It is shown from figure 12 that the flow field is highly anisotropic. The magnitude of largest u' is about 3 times larger than that of v', 5 times larger than that of w'. More importantly, the spatial distribution of velocity fluctuation is disparate for each velocity component. Large u' exists at the free surface, some distance from the centre-plane $y = 0$; large v' is located on the $y = 0$ plane at two depths, one at the free surface and the other some distance below; for w', the maximum value is located below the free surface and away from the centre-plane.

The statistics obtained here are used in the stability analysis and numerical simulations that follow. The mean profiles $U(y, z)$ are used to construct a base flow, while the distributions of the velocity fluctuation are directly compared to the predictions of the stability analyses and direct simulations.

4. Orr–Sommerfeld stability analysis

As observed in § 3.2, the meandering features observed behind the towed models are indicative of those associated with the instability of the free-surface wake. To investigate this, we perform a linear Orr–Sommerfeld (OS) stability analysis of the mean wake profiles obtained from the DPIV measurements. To obtain direct comparisons, we start with the Navier–Stokes equations and apply linearized free-surface boundary conditions corresponding to the same Reynolds and Froude numbers as in § 3.

https://doi.org/10.1017/S0022112002001684 Published online by Cambridge University Press

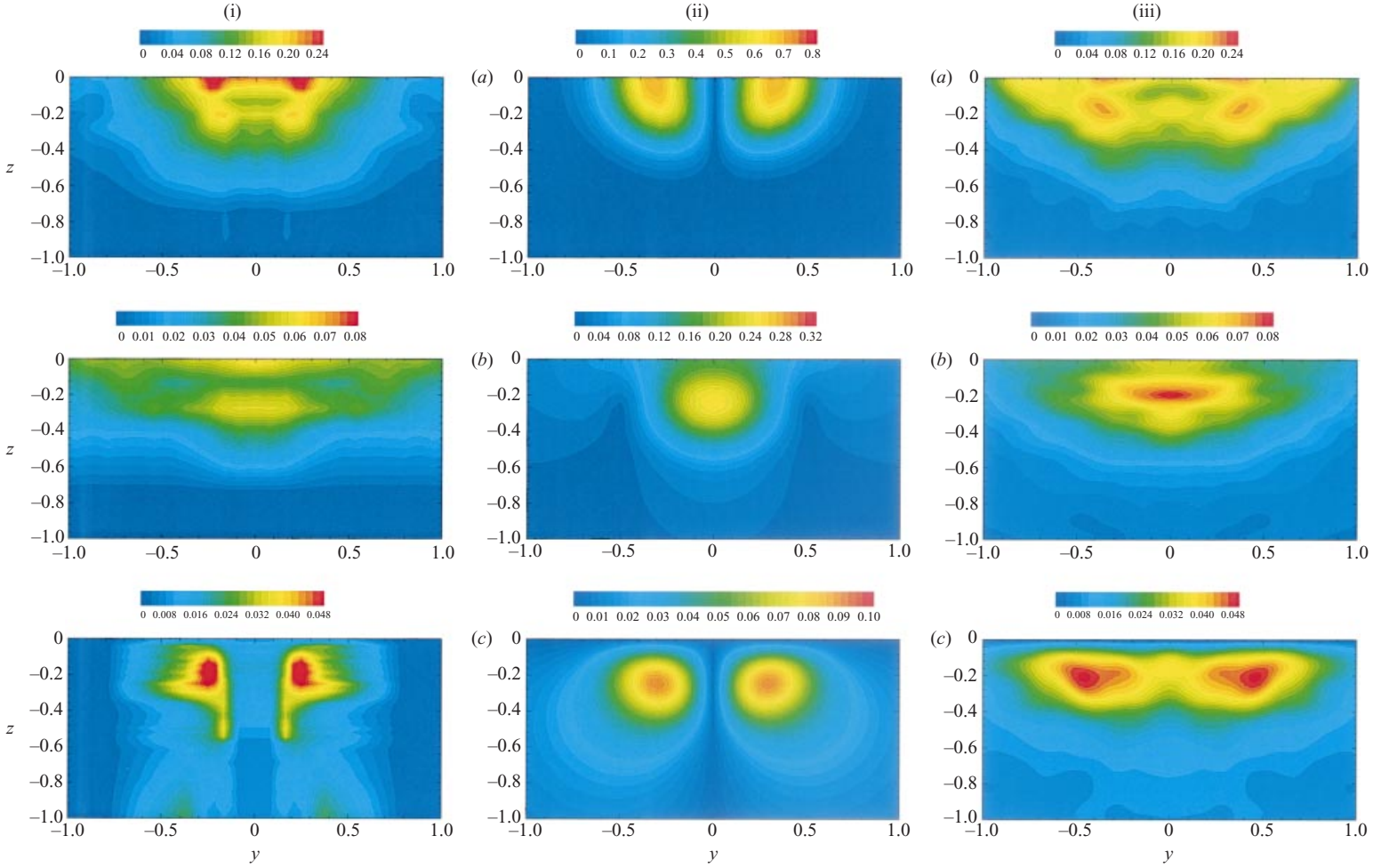

FIGURE 12. Contours of (a) streamwise velocity fluctuation $u'^{rms}(y,z)$, (b) lateral velocity fluctuation $v'^{rms}(y,z)$, and (c) vertical velocity fluctuation $w'^{rms}(y,z)$, obtained from: (i) DPIV, (ii) OS, and (iii) DNS. In DPIV, $X/b = 10$; in DNS, $t = 15$.

4.1. *Mathematical formulation*

Governing equations

For an incompressible, viscous, three-dimensional flow, the governing differential equations are Navier–Stokes equations:

$$\frac{\partial u_i}{\partial t} + u_j \frac{\partial u_i}{\partial x_j} = -\frac{\partial p}{\partial x_i} + \frac{1}{Re}\nabla^2 u_i, \tag{4.1}$$

and the continuity equation

$$\frac{\partial u_i}{\partial x_i} = 0, \tag{4.2}$$

where $(u_1, u_2, u_3) = (u, v, w)$ are the velocity components and p the dynamic pressure.

We assume that the wake flow consists of a mean parallel flow $U(y, z)$ and a perturbation part:

$$u = U(y, z) + u', \quad v = v', \quad w = w', \quad p = p', \quad \eta = \eta', \tag{4.3}$$

where η is the free-surface elevation. The linearized governing equations for the perturbation variables are obtained as

$$\frac{\partial u'}{\partial t} + U\frac{\partial u'}{\partial x} + v'\frac{\partial U}{\partial y} + w'\frac{\partial U}{\partial z} = -\frac{\partial p'}{\partial x} + \frac{1}{Re}\nabla^2 u', \tag{4.4}$$

$$\frac{\partial v'}{\partial t} + U\frac{\partial v'}{\partial x} = -\frac{\partial p'}{\partial y} + \frac{1}{Re}\nabla^2 v', \tag{4.5}$$

$$\frac{\partial w'}{\partial t} + U\frac{\partial w'}{\partial x} = -\frac{\partial p'}{\partial z} + \frac{1}{Re}\nabla^2 w', \tag{4.6}$$

$$\frac{\partial u'}{\partial x} + \frac{\partial v'}{\partial y} + \frac{\partial w'}{\partial z} = 0. \tag{4.7}$$

By taking divergency on both sides of equations (4.4)–(4.6) and invoking (4.7), we obtain the governing Poisson equation for the perturbed pressure p':

$$2\frac{\partial v'}{\partial x}\frac{\partial U}{\partial y} + 2\frac{\partial w'}{\partial x}\frac{\partial U}{\partial z} = -\nabla^2 p'. \tag{4.8}$$

By performing ∇^2 (4.5) and ∇^2 (4.6) and using (4.8), we finally obtain the governing equations for v' and w':

$$\left.\begin{aligned} \frac{\partial}{\partial t}(\nabla^2 v') + \nabla^2\left(U\frac{\partial v'}{\partial x}\right) &= \frac{\partial}{\partial y}\left(2\frac{\partial v'}{\partial x}\frac{\partial U}{\partial y} + 2\frac{\partial w'}{\partial x}\frac{\partial U}{\partial z}\right) + \frac{1}{Re}\nabla^4 v', \\ \frac{\partial}{\partial t}(\nabla^2 w') + \nabla^2\left(U\frac{\partial w'}{\partial x}\right) &= \frac{\partial}{\partial z}\left(2\frac{\partial v'}{\partial x}\frac{\partial U}{\partial y} + 2\frac{\partial w'}{\partial x}\frac{\partial U}{\partial z}\right) + \frac{1}{Re}\nabla^4 w'. \end{aligned}\right\} \tag{4.9}$$

Note that after v' and w' are solved, u' can be obtained from the continuity equation (4.7). We also remark that unlike in the two-dimensional case, the introduction of stream functions will not reduce equation number here. Hence, we continue with the primitive-variable formulations for the stability analysis.

Next we consider perturbations propagating parallel to the mean flow in the wavy form

$$f'(x, y, z, t) = \tilde{f}(y, z)\exp(\mathrm{i}(kx - \omega t)), \tag{4.10}$$

where $f(x, y, z, t)$ can be $u_i(x, y, z, t)$, $p(x, y, z, t)$ and $\eta(x, y, t)$. The governing equation

(4.9) finally becomes the OS equation

$$\left.\begin{aligned}
&\left[Uk\left(\frac{\partial^2}{\partial y^2}+\frac{\partial^2}{\partial z^2}-k^2\right)+2k\frac{\partial U}{\partial z}\frac{\partial}{\partial z}+k\left(\frac{\partial^2 U}{\partial z^2}-\frac{\partial^2 U}{\partial y^2}\right)\right.\\
&\qquad\left.+\frac{\mathrm{i}}{Re}\left(\frac{\partial^2}{\partial y^2}+\frac{\partial^2}{\partial z^2}-k^2\right)^2\right]\tilde{v}-\left(2k\frac{\partial U}{\partial y\partial z}+2k\frac{\partial U}{\partial z}\frac{\partial}{\partial y}\right)\tilde{w}\\
&\quad=\omega\left(\frac{\partial^2}{\partial y^2}+\frac{\partial^2}{\partial z^2}-k^2\right)\tilde{v},\\
&\left[Uk\left(\frac{\partial^2}{\partial y^2}+\frac{\partial^2}{\partial z^2}-k^2\right)+2k\frac{\partial U}{\partial y}\frac{\partial}{\partial y}+k\left(\frac{\partial^2 U}{\partial y^2}-\frac{\partial^2 U}{\partial z^2}\right)\right.\\
&\qquad\left.+\frac{\mathrm{i}}{Re}\left(\frac{\partial^2}{\partial y^2}+\frac{\partial^2}{\partial z^2}-k^2\right)^2\right]\tilde{w}\\
&\qquad-\left(2k\frac{\partial U}{\partial y\partial z}+2k\frac{\partial U}{\partial y}\frac{\partial}{\partial z}\right)\tilde{v}=\omega\left(\frac{\partial^2}{\partial y^2}+\frac{\partial^2}{\partial z^2}-k^2\right)\tilde{w},
\end{aligned}\right\}\tag{4.11}$$

which represents an eigenvalue problem with the eigenvalue $\omega = \omega_r + \mathrm{i}\omega_i$ and eigenvectors $\tilde{v}$ and $\tilde{w}$. From (4.10), positive ω_i leads to growing perturbations, which indicate instability.

Free-surface boundary conditions

At the free surface, consistent with the low Froude number in the wake flow considered here, we apply linearized kinematic and dynamic boundary conditions at $z = 0$ (cf. Shen *et al.* 1999):

$$\frac{\partial \eta}{\partial t}+\frac{\partial (u\eta)}{\partial x}+\frac{\partial (v\eta)}{\partial y}-w=0,\tag{4.12}$$

$$p-\frac{\eta}{Fr^2}-\frac{2}{Re}\frac{\partial w}{\partial z}=0,\tag{4.13}$$

$$\frac{1}{Re}\left(\frac{\partial u}{\partial z}+\frac{\partial w}{\partial x}\right)=0,\tag{4.14}$$

$$\frac{1}{Re}\left(\frac{\partial v}{\partial z}+\frac{\partial w}{\partial y}\right)=0.\tag{4.15}$$

Here the kinematic boundary condition (4.12) states that no particle leaves the free surface, while the dynamics boundary conditions (4.13)–(4.15) indicate the stress balance across the free surface.

By using the decomposition (4.3), we obtain the linearized free-surface boundary conditions for perturbations:

$$\frac{\partial \eta'}{\partial t}+U\frac{\partial \eta}{\partial x}-w'=0,\tag{4.16}$$

$$p'-\frac{\eta'}{Fr^2}-\frac{2}{Re}\frac{\partial w'}{\partial z}=0,\tag{4.17}$$

$$\frac{\partial u'}{\partial z}+\frac{\partial w'}{\partial x}=0,\tag{4.18}$$

$$\frac{\partial v'}{\partial z}+\frac{\partial w'}{\partial y}=0.\tag{4.19}$$

To be consistent with the governing OS equation (4.11) which does not contain p' and u', we next seek simplified free-surface boundary conditions. By performing $\partial/\partial x$ on both sides of (4.18) and invoking (4.19) and (4.7), we eliminate u':

$$\frac{\partial^2 w'}{\partial y^2} + \frac{\partial^2 w'}{\partial x^2} - \frac{\partial^2 w'}{\partial z^2} = 0. \tag{4.20}$$

The pressure p' in (4.17) is eliminated as follows. We first take $(\partial^2/\partial x^2 + \partial^2/\partial y^2)$ of (4.17) and obtain

$$\frac{\partial^2 p'}{\partial x^2} + \frac{\partial^2 p'}{\partial y^2} - \frac{1}{Fr^2}\left(\frac{\partial^2}{\partial x^2} + \frac{\partial^2}{\partial y^2}\right)\eta' - \frac{2}{Re}\left(\frac{\partial^2}{\partial x^2} + \frac{\partial^2}{\partial y^2}\right)\frac{\partial w'}{\partial z} = 0. \tag{4.21}$$

Next we introduce $\partial/\partial x$ of (4.4) and $\partial/\partial y$ of (4.5) into the above equation. By using the continuity equation (4.7) and the fact that $\partial U/\partial z = 0$ (there is no mean shear at the free surface), we finally obtain

$$\left(\frac{\partial}{\partial t} + U\frac{\partial}{\partial x}\right)\frac{\partial w'}{\partial z} - 2\frac{\partial v'}{\partial x}\frac{\partial U}{\partial y} - \frac{1}{Fr^2}\left(\frac{\partial^2}{\partial x^2} + \frac{\partial^2}{\partial y^2}\right)\eta' - \frac{1}{Re}\left(3\frac{\partial^2}{\partial x^2} + 3\frac{\partial^2}{\partial y^2} + \frac{\partial^2}{\partial z^2}\right)\frac{\partial w'}{\partial z} = 0. \tag{4.22}$$

For the wavy disturbance (4.10), boundary conditions (4.16), (4.22), (4.20) and (4.19) become

$$kU\tilde{\eta} + \mathrm{i}\tilde{w} = \omega\tilde{\eta}, \tag{4.23}$$

$$\frac{\mathrm{i}}{Fr^2}\left(\frac{\partial^2}{\partial y^2} - k^2\right)\tilde{\eta} + \left[kU + \frac{\mathrm{i}}{Re}\left(3\frac{\partial^2}{\partial y^2} + \frac{\partial^2}{\partial z^2} - 3k^2\right)\right]\frac{\partial}{\partial z}\tilde{w} - 2k\frac{\partial U}{\partial y}\tilde{v} = \omega\frac{\partial \tilde{w}}{\partial z}, \tag{4.24}$$

$$\left(\frac{\partial^2}{\partial y^2} - \frac{\partial^2}{\partial z^2} - k^2\right)\tilde{w} = 0, \tag{4.25}$$

$$\frac{\partial \tilde{w}}{\partial y} + \frac{\partial \tilde{v}}{\partial z} = 0. \tag{4.26}$$

Numerical implementation

By using a fourth-order finite-difference scheme, the governing OS equation (4.11) is solved as an eigenvalue problem subject to the free-surface boundary conditions (4.23)–(4.26) and free-slip boundary conditions at the bottom $z = -L_z$. In the transverse direction far away, $y = \pm L_y/2$, a zero-disturbance condition is used.

Because of the symmetry of the mean flow U about the centre-plane $y = 0$, and because of the linearity of this problem, we can decompose the disturbance into a symmetric mode and an anti-symmetric mode. For the symmetric mode, u', w', p' and η' are symmetric about $y = 0$ and v' is anti-symmetric, while for the anti-symmetric mode the opposite holds. This decomposition reduces the computation domain by half and facilitates the numerical calculation.

To solve for the OS equation, we need the value and spatial derivatives of the mean velocity at all the grid points. To obtain these from DPIV measurements (on discrete planes and at a relatively small number of points, cf. figure 11*a*), we fit an analytical form to the data:

$$U(y,z) \approx -U_0 \exp(-\sigma y^2)\cosh^{-2}(\gamma z). \tag{4.27}$$

Here U_0 is the maximum velocity deficit; σ and γ are parameters specifying the spatial

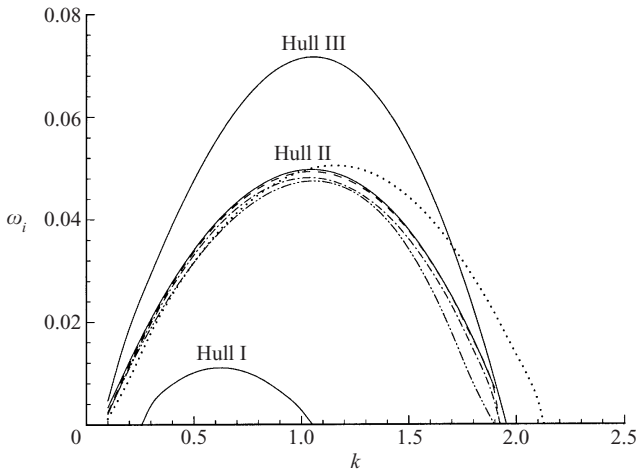

FIGURE 13. OS growth rate ω_i as a function of wavenumber k for hulls I, II and III. For hull II ———, $L_y = 4$, $L_z = 2$, $N_y = 24$, $N_z = 64$; - - - - -, $L_y = 4$, $L_z = 2$, $N_y = 18$, $N_z = 48$; · · · · · · ·, $L_y = 4$, $L_z = 2$, $N_y = 12$, $N_z = 32$; – · – · –, $L_y = 6$, $L_z = 2$, $N_y = 24$, $N_z = 64$; —··—··—, $L_y = 4$, $L_z = 3$, $N_y = 24$, $N_z = 64$.

expansion of the wake flow. For the case shown in figure 11(*a*), a least-square best fit is obtained with $U_0 = 0.85$, $\sigma = 3.09$, and $\gamma = 2.85$. The analytical profile (4.27) with these values is plotted in figure 11(*b*). The agreement with the data in figure 11(*a*) is excellent (with a correlation coefficient of $\sim 98\%$).

In the OS solver, we use a $N_y \times N_z = 24 \times 64$ grid for a computational domain size $L_y/2 \times L_z = 2 \times 2$. The choice of these parameters is justified in the convergence tests for the hull II case shown in figure 13, where the growth rates for anti-symmetric modes ω_i are plotted as a function of wavenumber k. We first fix the domain size and vary the grid resolution. It shows clearly that as the grid becomes finer, the solution converges fast and the current 24×64 grid is sufficient. We then test different domain size with the grid number fixed. The fact that the variation in domain size changes the results only in a negligible way shows that our domain size is large enough such that the effects of far boundaries are small.

Note that compared to that in the y-direction, the resolution in the z-direction is much finer. This is necessitated by the requirement to resolve the free-surface boundary layer accurately, which is discussed in § 5. We remark again that the same $Re = 1000$ and $Fr = 0.04$ as the experiments are used in the stability analysis.

4.2. *Results*

The OS equations are solved at different wavenumbers k. It is found that instability is caused by anti-symmetric modes, which directly correspond to the meandering pattern observed from DPIV measurement. Figure 14 shows such an example. The unstable mode at $k = 1.0$ for hull II with the maximum velocity fluctuation magnitude $0.1U_0$ is plotted in figure 14(*a*). The anti-symmetry about $y = 0$ and the sinusoidal variation in the x-direction are clearly shown. When superimposed upon the mean flow, we obtain the surface contours of u plotted in figure 14(*b*) which resemble the experimental observation (figure 5*b*).

Figure 13 shows the growth rate ω_i as a function of wavenumber k for all three hulls. As a key result, we observe that the instability region and the growth rates of unstable modes are highly dependent on the hull geometry. The wake of the

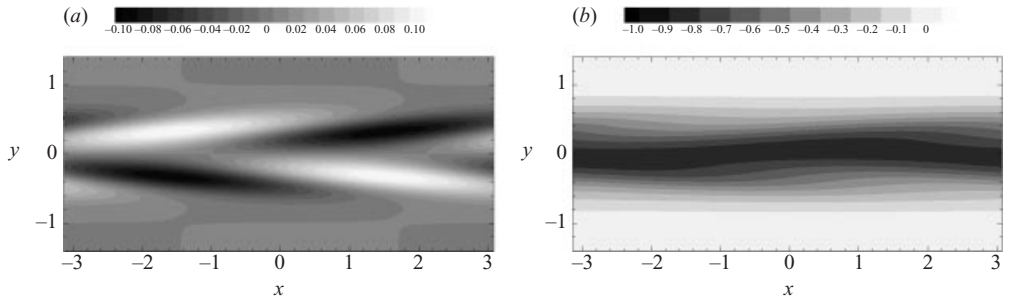

FIGURE 14. Surface contours of streamwise velocity u: (a) obtained from the OS unstable mode at $k = 1.0$, with the maximum velocity fluctuation magnitude $0.1U_0$; and (b) superimposition of the OS unstable mode upon the mean flow.

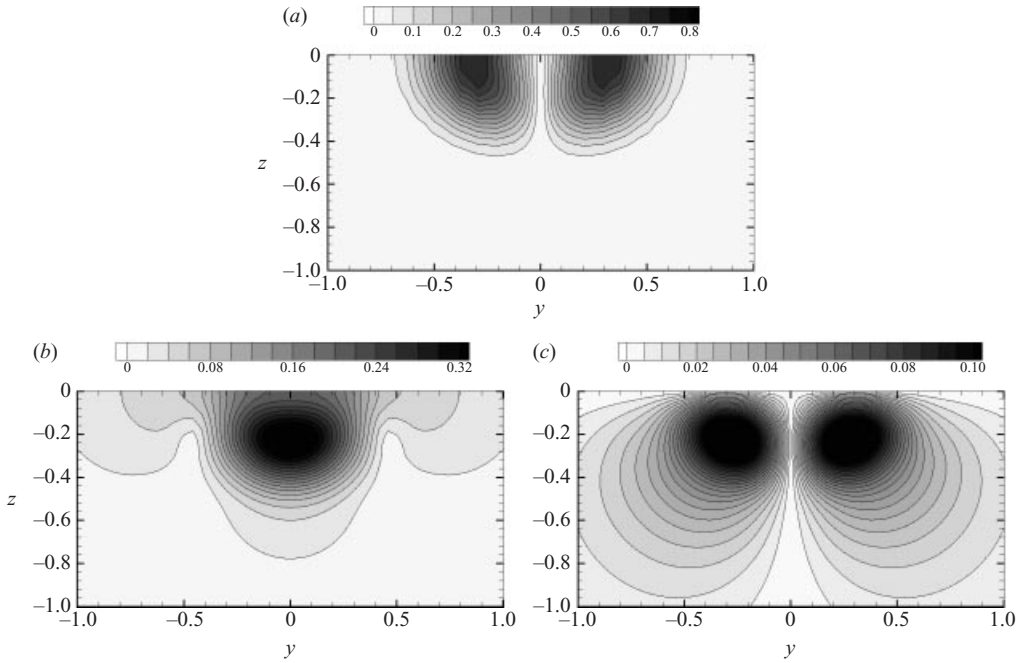

FIGURE 15. Contours of the OS unstable modes of velocity components: (a) $u'^{rms}(y,z)$, (b) $v'^{rms}(y,z)$, and (c) $w'^{rms}(y,z)$ for $k = 1.5$.

shallow hull (hull I) has a relatively small portion of unstable wavenumbers with low growth rates. The wake flows for the circular (hull II) and deep (hull III) hulls are much more unstable; of the two, the unstable modes for hull III grow faster. These results are consistent with the experimental observations shown in figures 6 and 10 in terms of the meandering prominence and lateral amplitude. From figure 13 we observe that the most unstable modes for hulls II and III occur at $k_{max} \approx 1.0$ and 1.1, corresponding to $L_{max} \approx 6.3$ and 5.7 respectively. These compare qualitatively (only) to the experimentally determined values of $L_m \sim 4$ for the two hulls. Clearly, the OS prediction does not capture the nonlinear processes in the (subsequent) evolution of the turbulent wake.

Figures 12(ai)–12($c$ii) plot the spatial distributions of the most unstable mode (at $k = 1$) for each velocity component. Here and hereafter, the magnitude of a

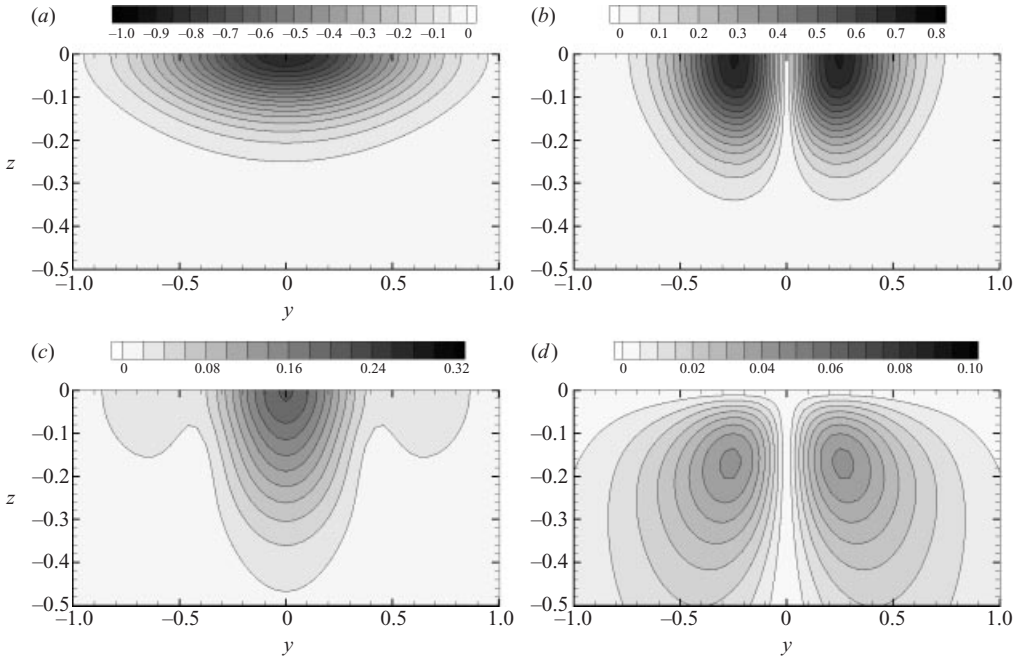

FIGURE 16. Contours of (*a*) mean velocity $U(y,z)$ and the OS unstable modes for velocity components: (*b*) $u'^{rms}(y,z)$, (*c*) $v'^{rms}(y,z)$, and (*d*) $w'^{rms}(y,z)$ for hull I. $k = 0.6$.

velocity component of an unstable mode is defined as $u_i'^{rms} = |\,\widetilde{u}_i\,|/\sqrt{2}$ (cf. (4.10)) and is normalized to satisfy $u_i'u_i'|_{max} = 1$. Since the mode is anti-symmetric, maximum u' and w' are located some distance from the centre-plane while maximum v' occurs at $y = 0$. Vertically, maximum u' occurs at the free surface, while maximum v' and w' are below the surface. Among the three components, u' has the largest magnitude while w' is smallest. These features are completely consistent with those obtained in the DPIV measurements (figures 12*a*i–12*c*i).

It is of interest to plot (in figure 15) the spatial distributions of the unstable mode at wavenumber $k = 1.5$ corresponding to the experimentally determined value of $L_m \approx 4.1$. Comparing with figures 12(*a*ii)–12(*c*ii), the distributions are very similar and the mode shapes do not appear to be sensitive to the wavenumber.

Finally, we consider the effects of b/d on the unstable mode shape. These are plotted in figures 16 and 17, respectively for hulls I and III. Comparing these with figures 12(*a*ii)–12(*c*ii), we see that the effect of the aspect ratio of the wake is mainly in the vertical distribution which scales approximately with the base flow. Except for the fact that v' for hull I has its maximum at the free surface, the overall difference between the three hull geometries is small. This, together with the aforementioned insensitivity of the unstable mode distribution to the wavenumber, leads to the conclusion that the shape of the unstable modes obtained here is generic for such wake flows. The growth rate, on the other hand, may differ substantially as shown in figure 13.

The present Orr–Sommerfeld analysis provides strong evidence that the meandering features observed in the experiments are initiated by the inherent instability of the mean wake. The evolution leading to the final flow involves nonlinear processes not present in the analysis. These are included in the direct numerical simulations which we describe in the next section.

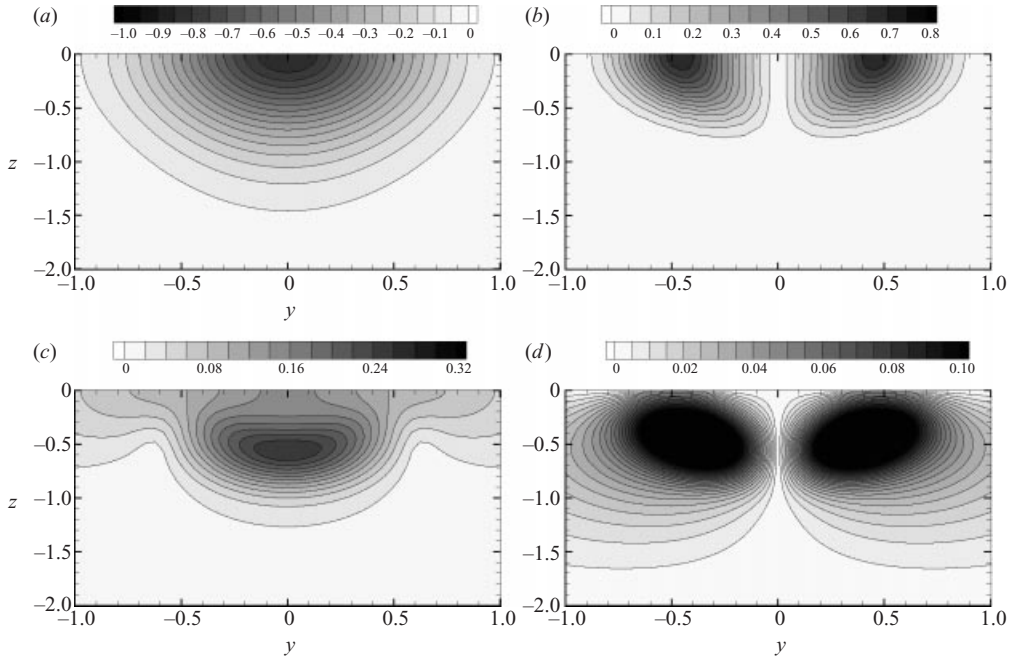

FIGURE 17. Contours of (*a*) mean velocity $U(y,z)$ and the OS unstable modes for velocity components: (*b*) $u'^{rms}(y,z)$, (*c*) $v'^{rms}(y,z)$, and (*d*) $w'^{rms}(y,z)$ for hull III. $k = 1.0$.

5. Direct numerical simulations

To understand the generation and development of the wake features and to obtain quantitative comparisons with measurement, we perform direct numerical simulations (DNS) of the evolution of the turbulent wake. To aid the understanding of the underlying mechanisms, DNS also provides detailed information about the three-dimensional flow field and statistics only partially available from DPIV.

5.1. *Numerical method*

In DNS, the Navier–Stokes equations (4.1) together with the continuity equation (4.2) are solved using finite-difference discretizations. We use a sixth-order finite-difference scheme in the horizontal directions and a second-order scheme in the vertical direction. The Navier–Stokes equations are marched in time using a second-order Runge–Kutta scheme. At each timestep, the pressure is solved via a Poisson equation, which is obtained by taking divergence of the Navier–Stokes equations and invoking the continuity equation. The details of the numerical algorithm are provided in Shen *et al.* (1999).

At the free surface, the (linearized) kinematic boundary condition (4.12) and dynamic boundary conditions (4.13)–(4.15) are applied, while at the bottom of the domain, we use a free-slip condition. By assuming that longitudinal variations of flow statistics over the domain length L_x are small, and that turbulence correlations (except for the meandering) are negligible over half of the domain, we employ a periodic condition in the horizontal directions.

The computational domain sizes are $L_z = 2$ vertically, $L_y = 4$ laterally, and $L_x = 3.33\pi$, 2π and 1.82π streamwise for hulls I, II and III, respectively. The streamwise lengths of each hull correspond to the wavelengths of their most unstable modes found in the Orr–Sommerfeld analysis (figure 13). We use a 128 (streamwise) $\times$

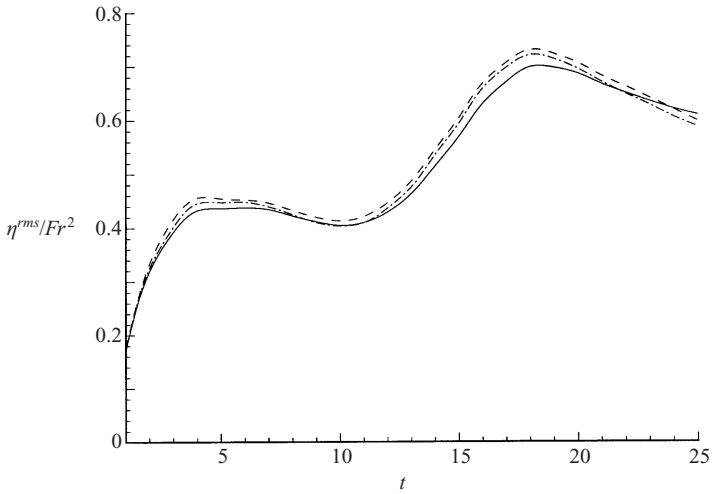

FIGURE 18. Time evolution of free-surface elevation obtained from DNS with: a $128 \times 96 \times 128$ grid (———), a $64 \times 48 \times 64$ grid (- - - - -), and a $64 \times 48 \times 64$ grid with fully-nonlinear free-surface boundary conditions (– · – · –).

96 (lateral) × 128 (vertical) grid. With a timestep 0.005, the simulations are carried out from $t = 0$ to 25.

Careful validation has been performed to ensure that the present numerical approach obtains converged results with all the dynamically significant scales resolved (cf. Shen *et al.* 1999). Based on viscosity and kinetic energy dissipation rate, the Kolmogorov scale is estimated to be around 0.02, which is close to the grid resolution of our DNS. Figure 18 shows another example, where the time evolution of free-surface elevation η^{rms} is examined. When the number of grid points in each dimension is reduced by a factor of 2, the resulting change in η^{rms} is small. This shows that the current grid resolution is sufficient. Figure 18 also compares the results of the present numerical method using linearized free-surface boundary conditions with a numerical scheme with fully nonlinear free-surface boundary conditions (cf. Zhang 1996). The negligible difference in η^{rms} justifies the free-surface linearization. Under the present experimental conditions, $Fr = 0.04$, a small effect of free-surface deformation is expected (η^{rms} scales as Fr^2 at low Froude numbers). In an earlier study (Shen *et al.* 1999), it is found that for low Froude numbers, the difference between a deformable free surface and a free-slip plate is small except for the pressure–strain correlation in the Reynolds-stress evolution.

As a cross-validation between DNS and OS analysis, we perform numerical simulations for the interaction between the mean flow and the unstable modes obtained in §4. Figure 19 compares the growth rates of the unstable modes with the theoretical prediction $\exp(\omega_i t)$. For each hull geometry, we initially input the most unstable mode with the maximum magnitude 10% of the mean flow deficit. As indications of mode growth, we examine the maximum values of the fluctuations of each velocity component $u'^{rms}_{i,max}$ as well as the averaged fluctuation kinetic energy

$$E_f \equiv \frac{1}{L_y L_z} \int_{-L_z}^{0} \int_{-L_y/2}^{L_y/2} \frac{u'^2 + v'^2 + w'^2}{2} \, \mathrm{d}y \, \mathrm{d}z. \tag{5.1}$$

As shown in figure 19, for all three hull geometries and for all the quantities examined, the growth of unstable modes agrees well with the theoretical prediction (the

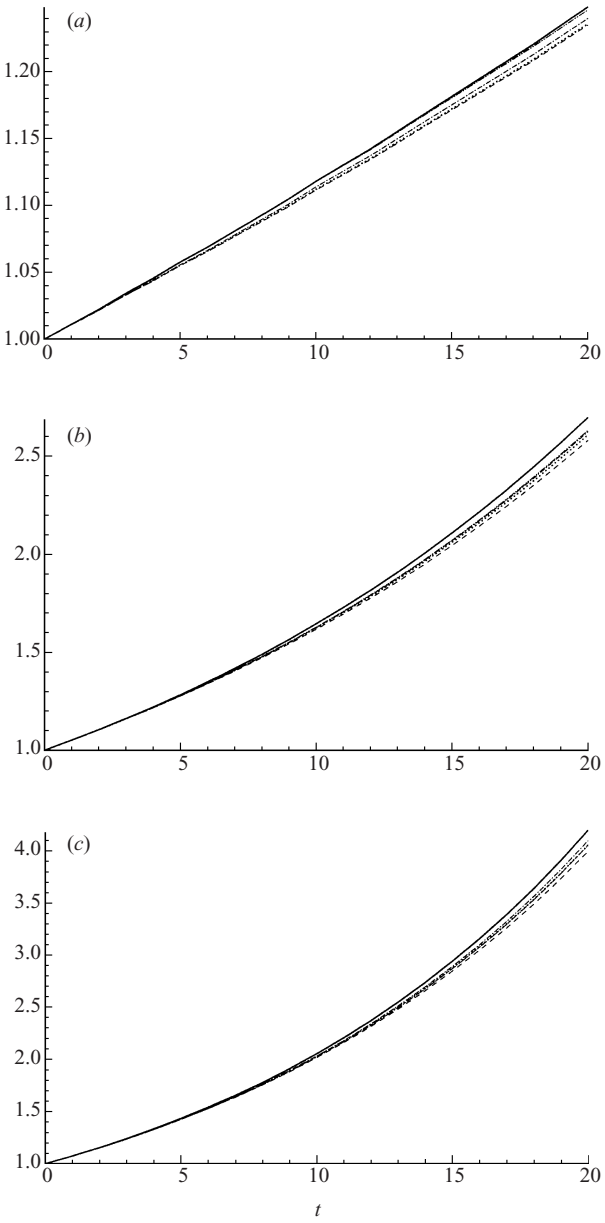

FIGURE 19. Comparison of the growth rates of unstable modes between OS prediction $\exp(\omega_i t)$ (———) and DNS results of: $u'^{rms}_{max}(t)$ (- - - - -), $v'^{rms}_{max}(t)$ (– · – · –), $w'^{rms}_{max}(t)$ (— ·· — ·· —), and $E_f(t)$ (· · · · · · ·), for (*a*) hull I, (*b*) hull II, and (*c*) hull III. DNS results are normalized by initial values.

errors are within 4%). Considering the substantial difference between the numerical discretization schemes of the OS analysis and DNS, this agreement is excellent and the two studies cross-validate each other.

5.2. *Initial condition*

To perform a direct quantitative comparison between the experimental measurements and numerical simulations, an essential task is the construction of the initial flow field

for simulations. A desirable approach is to match the initial field as closely as possible to the experimental measurements at an early stage, let the DNS run for some time, and then compare the numerical result to the experimental measurements at a later stage. A typical example is the simulation of grid turbulence by Kwak, Reynolds & Ferziger (1975), where the turbulence fluctuation intensity and energy spectrum are initially matched and finally compared to wind-tunnel measurements (Comte-Bellot & Corrsin 1971).

This approach of fully matching the initial condition to experimental input, however, is limited to flows with a simple configuration. As shown in § 3, the turbulent wakes behind the ship models are rather complicated. The velocity field is highly anisotropic and heterogeneous: the magnitude of u' is generally much larger than that of v' and w', while the spatial distributions of the fluctuation magnitudes of each velocity component are substantially different; the variations in the lateral and vertical directions are large; in the streamwise direction, although quasi-homogeneity can be assumed, the presence of meandering complicates the representation of fluctuation distribution. Considering all these facts, the full construction of the initial wake field based on limited experimental inputs is a formidable task.

We adopt an alternative approach for the construction of the initial field: at $t = 0$ we match only the mean velocity profile to the experimental measurement, by using the expression (4.27). For turbulence fluctuations, we simply add to the mean flow a divergence-free random velocity noise, with the fluctuation profile proportional to a prescribed function

$$F(y, z) = \exp(-\sigma y^2)\cosh^{-2}(\gamma z)\tanh(\gamma z), \tag{5.2}$$

which is chosen to constrain the fluctuation within the wake and to forbid initial fluctuation at the free surface. This velocity noise serves only as the seeds for turbulence, and it is expected that real turbulence will develop as the simulation proceeds. After becoming fully developed, the flow field will then be compared to experimental measurements.

An interesting issue in setting up the DNS initial condition is the seeding for the eventual development of the wake meandering. Based on the experimental observation in § 3 and the stability analysis in § 4, we expected that a wake that is initially homogenous in the streamwise direction will, in time, develop distinct meandering features. The time required for this development depends on the (initial) noise in the turbulence flow and the growth rate of the unstable mode(s). For practical purposes, this process can be modelled in the DNS by the initial introduction of small-amplitude unstable mode(s).

In the present DNS, the initial velocity field is constructed using a superposition of three components:

$$u_i^{\text{initial}} = u_i^{\text{mean}} + \varepsilon^{\text{ran}} u_i^{\text{ran}} + \varepsilon^{\text{OS}} u_i^{\text{OS}}, \tag{5.3}$$

where u_i^{mean} is the mean flow given by (4.27), u_i^{ran} the random turbulence seeds, and u_i^{OS} the unstable mode obtained from OS analysis. For definiteness, we normalize u_i^{ran} and u_i^{OS} such that their maximum fluctuation magnitudes are of unit value, while ε^{ran} and ε^{OS} are small parameters. In the present study we choose $\varepsilon^{\text{OS}} = 0.1$ and $\varepsilon^{\text{ran}} = 0.088$. The value of ε^{OS} is somewhat arbitrary and primarily (with ε^{ran}) determines the time and position offset between DNS and DPIV that offers a good fit (see figure 7). The value of ε^{ran} is selected based on a fitting of the evolution of the

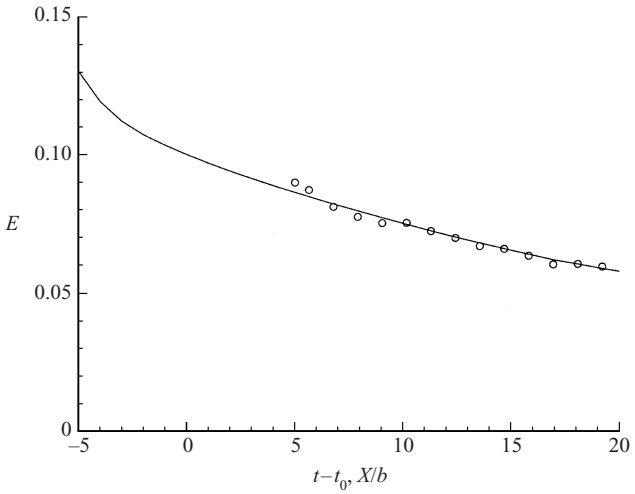

FIGURE 20. Comparison of time evolution of total kinetic energy between DNS (———) and DPIV (○). $t_0 \approx 5.0$.

total kinetic energy

$$E \equiv \frac{1}{L_x L_y L_z} \int_{-L_z}^{0} \int_{-L_y/2}^{L_y/2} \int_{-L_x/2}^{L_x/2} \frac{u^2 + v^2 + w^2}{2} \, \mathrm{d}x \, \mathrm{d}y \, \mathrm{d}z \tag{5.4}$$

between the DNS and the DPIV. With these values of the two small parameters, a reasonable (an explicit optimization is not performed) fit is obtained with a DNS time offset of $t_0 \approx 5.0$ where $(X/b)_{\mathrm{DPIV}} = (t - t_0)_{\mathrm{DNS}}$. With this offset, the comparison of the evolution of E is shown in figure 20. The comparison is excellent. Hereafter we compare the DPIV/DNS results at $(X/b)_{\mathrm{DPIV}} = (t - t_0)_{\mathrm{DNS}} = 10$ (i.e. at $t_{\mathrm{DNS}} = 15$), when the turbulent field has fully developed in the simulation.

5.3. *Numerical results*

Turbulence statistics

Figures 12(*a*iii)–12(*c*iii) plot the fluctuation profiles for each velocity component obtained from DNS. Note that as pointed out in § 5.2, the initial distribution of velocity fluctuations is non-physical (not plotted here) and serves only as the seed for the development of turbulence. As the simulation continues, real turbulence develops. It is shown in figure 12(iii) that at $t = 15$, large u' exists near the free surface, at the two sides of the centre-plane $y = 0$; large w' is also located at some distance from the centre-plane, but below the free surface; v' has its maximum value below the surface on $y = 0$. Comparing this to figures 12(i) and 12(ii), it is found that the numerical results agree well with experimental measurement and stability analysis in both the magnitude and spatial variation of the fluctuations for all the velocity components. A small but discernible difference between the DNS and the DPIV and OS results is that the velocity maxima of the former are at a greater distance from the centre-plane. This can be explained since in the DNS there is additional time (the offset time t_0 discussed in § 5.2) for lateral diffusion to occur.

Figure 21 plots the contours of vorticity fluctuations. In the bulk flow below, the difference between $\omega_x'^{rms}$, $\omega_y'^{rms}$ and $\omega_z'^{rms}$ is relatively small, especially when compared to the velocity field which is highly anisotropic. Near the free surface, however, the

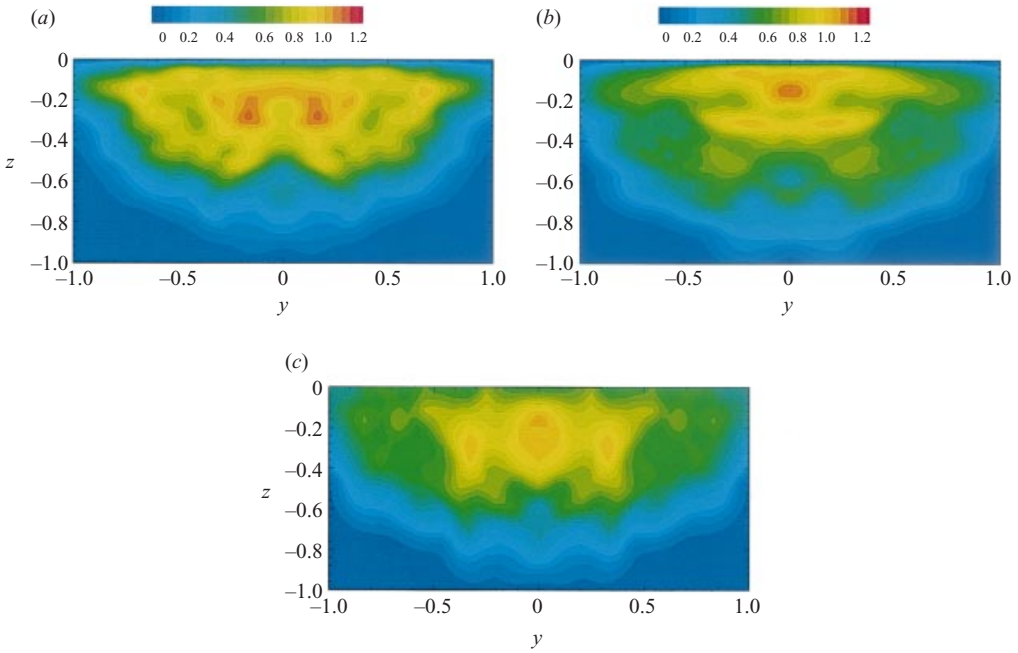

FIGURE 21. Contours of fluctuations of vorticity components obtained from DNS: (*a*) $\omega_x'^{rms}$; (*b*) $\omega_y'^{rms}$; (*c*) $\omega_z'^{rms}$. $t = 15$.

fluctuations have disparate behaviours for different vorticity components: $\omega_x'^{rms}$ and $\omega_y'^{rms}$ decrease dramatically over a thin region adjacent to the surface, while the vertical variation of $\omega_z'^{rms}$ diminishes at the surface (the contours lines of $\omega_z'^{rms}$ are perpendicular to the free surface in figure 21*a*). This is because the free-surface zero-stress dynamic boundary condition together with the low Froude number require ω_x, ω_y and $\partial\omega_z/\partial z$ to vanish at the free surface (cf. Shen *et al.* 1999, 2000). The thin region where the free-surface viscous boundary conditions are felt is called the *free-surface inner layer*. The *free-surface outer layer* is the region over which the surface blockage effect associated with the free-surface kinematic boundary condition is felt. Over the outer layer, the vertical velocity component w decreases, as shown in figure 12(*c*).

The multi-layer structure of free-surface wakes is illustrated more clearly in figure 22, which plots the vertical variations of w'^{rms}, $\omega_x'^{rms}$ and $\omega_y'^{rms}$ at $y = 0$, -0.25, -0.5 and -0.75. Note that near the free surface, which is the focus of the present study, the statistics are well-resolved and converged. In the bulk flow region, more ensemble simulations may be required to obtain statistical convergence (as evident from the wavy variation). It is shown that the vanishing of w'^{rms}, $\omega_x'^{rms}$ and $\omega_y'^{rms}$ towards the free surface prevails for all the lateral locations examined. For this wake flow, the thicknesses of the inner and outer layers are approximately 0.05 (figure 22*a*) and 0.15 (figures 22*b* and 22*c*), respectively.

Finally we examine the turbulence length scales in the wake. For variables $f = u_i$, ω_i, the streamwise Taylor microscales are defined as

$$\lambda_f \equiv \sqrt{\frac{-2}{\partial^2 R_f(\xi)/\partial\xi^2|_{\xi=0}}}, \tag{5.5}$$

where the correlation function $R_f(\xi)$ is defined in (3.1). (Because of the meandering in

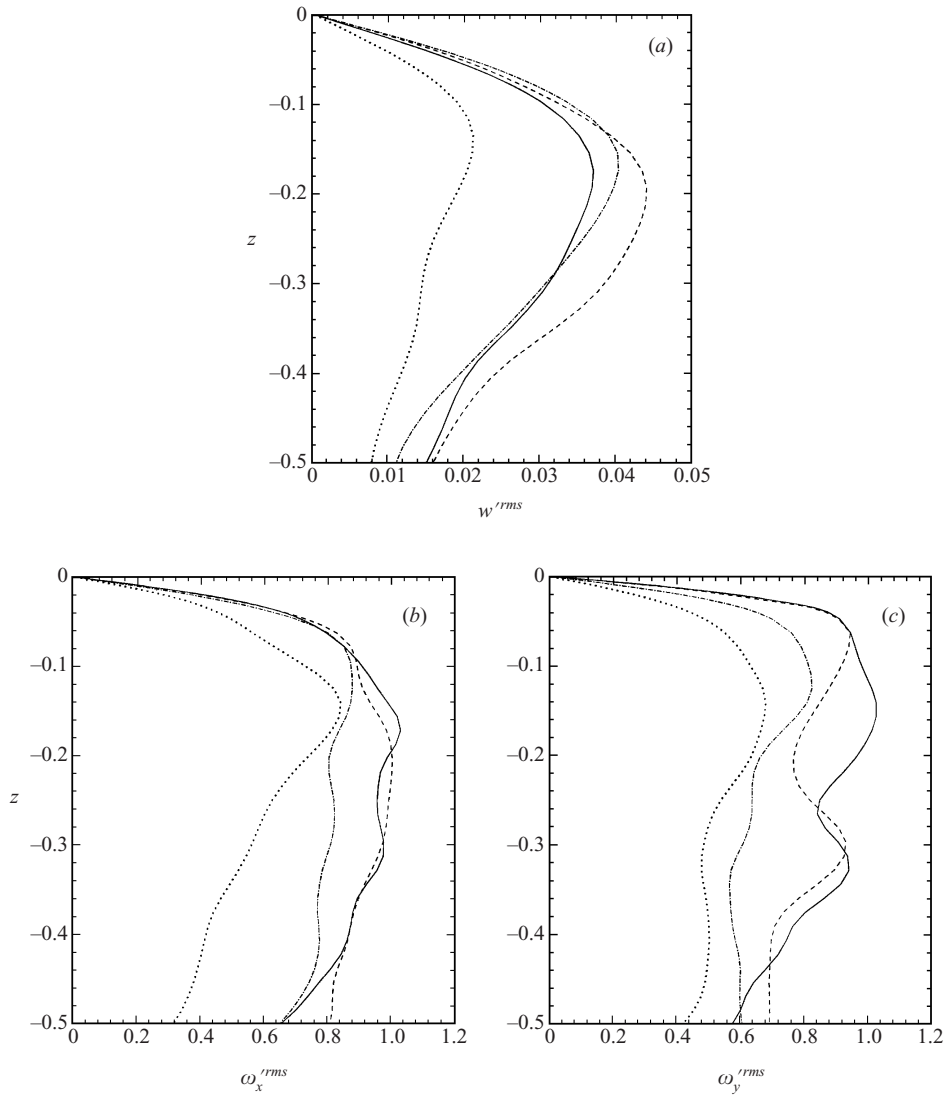

FIGURE 22. DNS profiles of (*a*) w'^{rms}; (*b*) $\omega_x'^{rms}$; and (*c*) $\omega_y'^{rms}$ at $y = 0$ (———), −0.25 (- - - - -), −0.5 (– · – · –), −0.75 (· · · · · · ·). Results are averaged over a lateral width 0.1. $t = 15$.

the wake, the macroscale, say defined by $\Lambda_f \equiv \int_0^{L_x/2} R_f(\xi)\,\mathrm{d}\xi$, tends to be dominated by L_m, and is not as useful in the present context.)

Figure 23 plots the contours of λ_{u_i} and λ_{ω_i}. It is shown that except for λ_u and λ_{ω_x}, which have maximum values along the periphery of the wake, the variation of microscales is relatively small in the flow below. As the free surface is approached, λ_w and λ_{ω_z} decrease while λ_{ω_x} and λ_{ω_y} increase. The former is related to the stretching of surface-connecting vortices, while the latter indicates the flattening of horizontal vortex structures as they impinge on the free surface. These phenomena have also been observed in other types of free-surface turbulent flows (cf. Handler *et al.* 1993 for open-channel flow and Shen *et al.* 1999 for the interaction between a shear flow and a free surface), and can be regarded as generic features of free-surface turbulence.

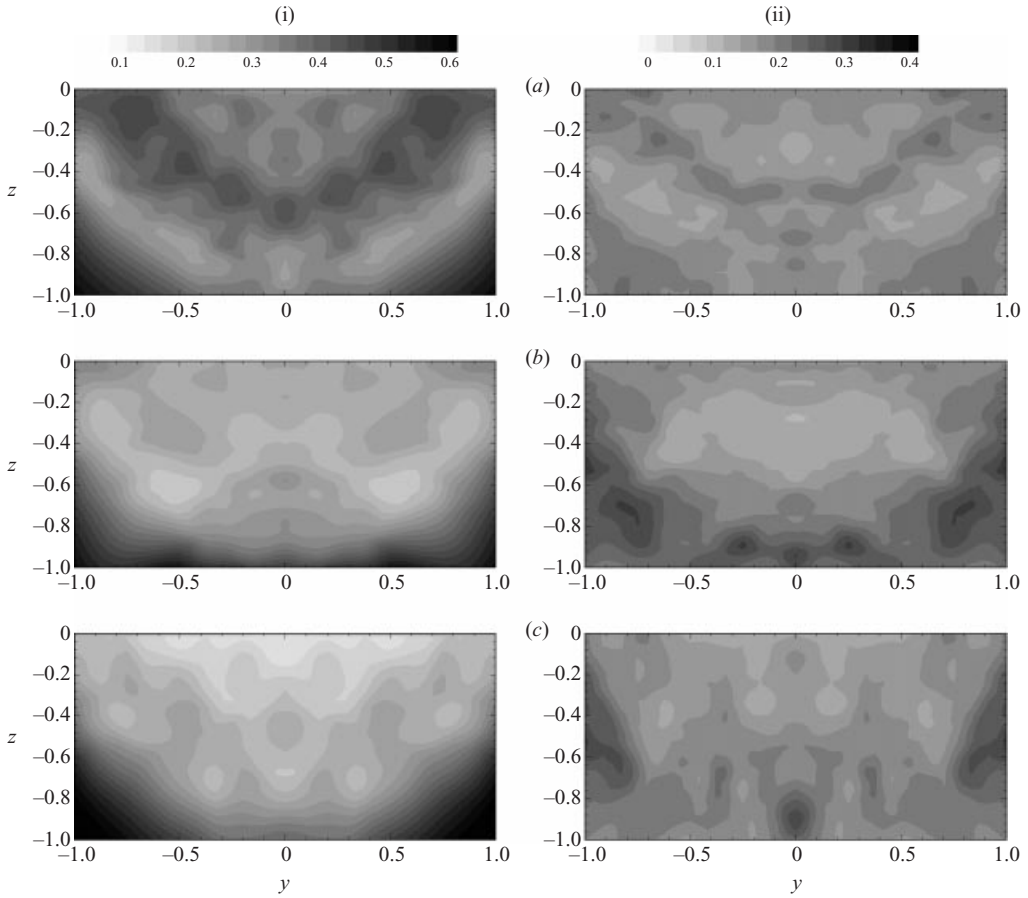

FIGURE 23. Contours of Taylor microscales for: velocity components (*a*i) λ_u, (*b*i) λ_v, (*c*i) λ_w; and vorticity components (*a*ii) λ_{ω_x}, (*b*ii) λ_{ω_y}, (*c*ii) λ_{ω_z}, obtained from DNS results at $t = 15$.

Turbulence structures

As shown in § 3, DPIV measures the two-dimensional instantaneous velocity field, which provides important insights into turbulence features in the wake. DNS, on the other hand, generates three-dimensional instantaneous datasets for all the physical variables computed. This greatly facilitates the illustration of turbulence structures in the wake, which we investigate next.

At the instant $t = 15$ when the wake turbulence has fully developed, figures 7(*a*ii)–7(*e*ii) plot ω_z contours at different depths corresponding the locations measured by DPIV. Comparing these with figures 7(*a*i)–7(*e*i), it is found that the DNS results agree with the experiment with remarkable accuracy (note that the spatial resolution of DNS is higher than that of DPIV and thus DNS provides more detailed structures). Figure 24(*c*) plots the surface ω_z contours at the same time. Comparison between figures 24(*c*) and 7(*a*ii) shows that the ω_z signature at $z = -0.05$ clearly resembles that at the free surface (the correlation coefficient is greater than 97%). This justifies the approach of approximating the surface ω_z feature by the near-surface one, which is used by the experimental study in § 3. Indeed, the ω_z contours preserve the same configuration at all the depths examined in figure 7(ii), except for the variation in

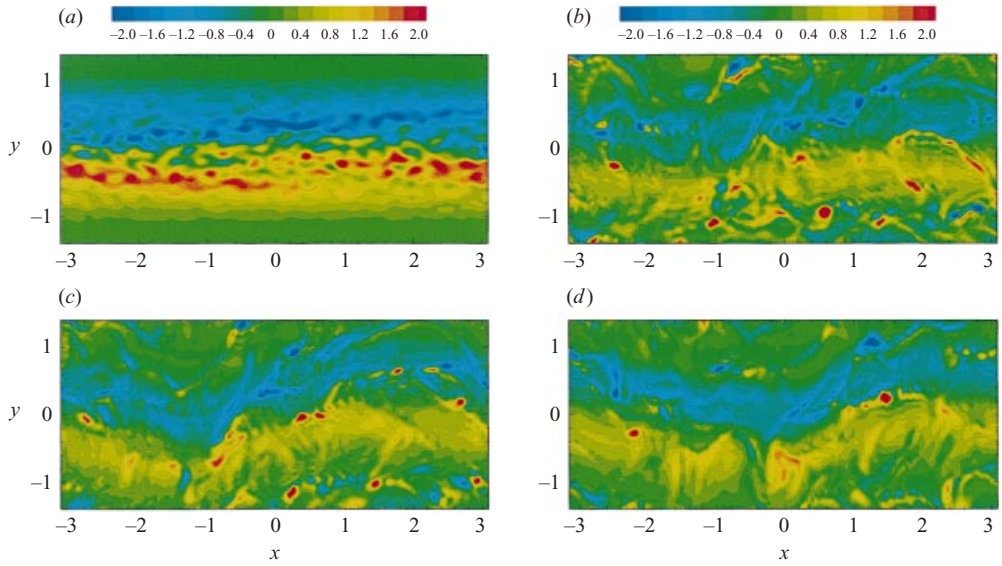

FIGURE 24. DNS surface contours of ω_z at: (*a*) $t = 0$, (*b*) 10, (*c*) 15, and (*d*) 20.

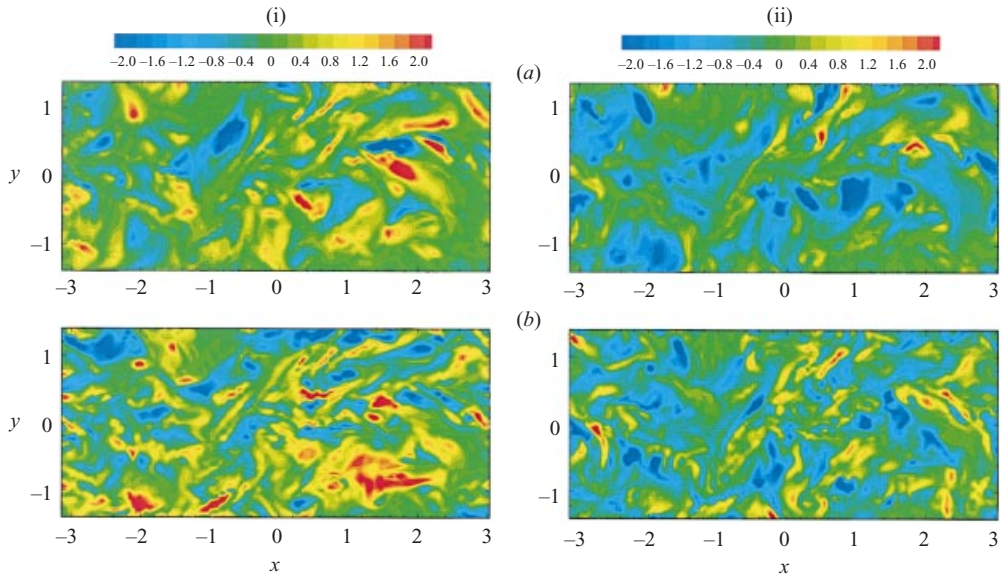

FIGURE 25. Contours of (*a*) ω_x and (*b*) ω_y at (i) $z = -0.03$ and (ii) $z = -0.13$, obtained from DNS results at $t = 15$.

magnitude. This suggests that surface-connected vortices are perpendicular to the free surface.

The features of horizontal components of vorticity, on the other hand, do not preserve their configuration as the depth changes. As shown in figure 25, ω_x and ω_y differ considerably at two planes separated by only a small distance 0.1.

The above scenario is elucidated more clearly in figure 26, where vortex lines of coherent vortex structures are plotted. To present the structures more clearly, we show here only selected structures. The surface-connected vortices, which are perpendicular

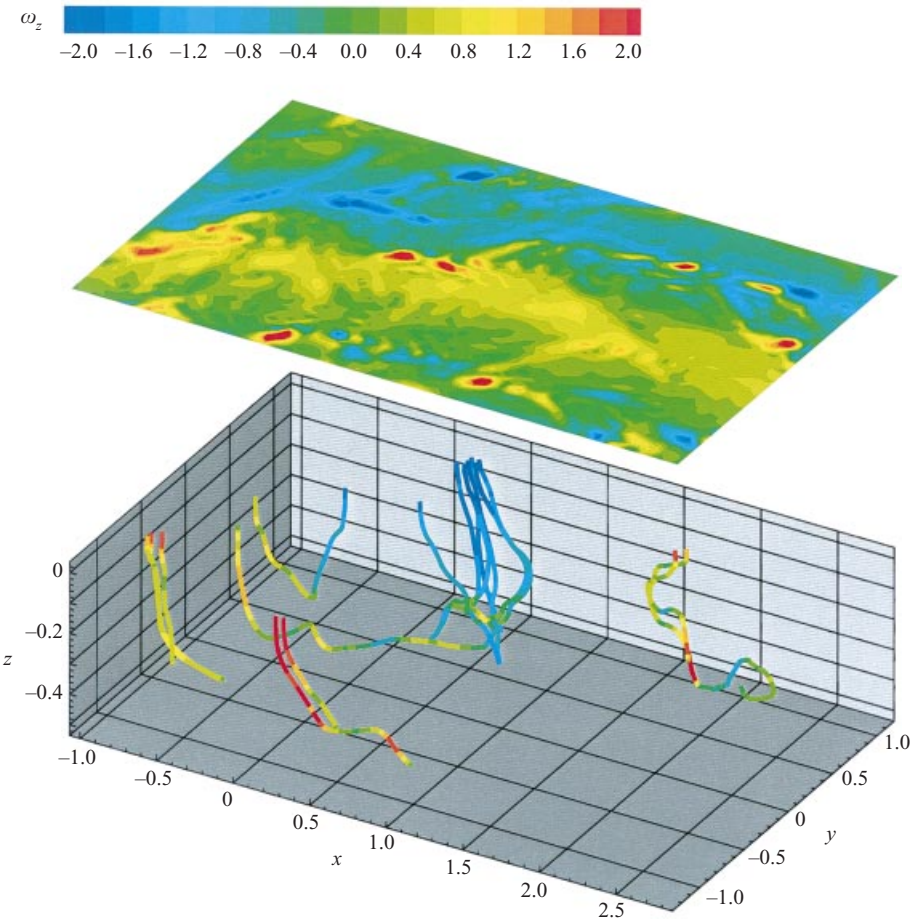

FIGURE 26. Free-surface ω_z contours and the vortex lines of underlying coherent vortex structures. $t = 15$.

to the free surface, are clear. They are found to be very persistent and are the most prominent surface signature of the wake flow. A careful examination shows that ω_z for surface-connected vortices decays at a slow rate closer to the laminar case than the turbulent one, in a way very similar to the shear-flow free-surface turbulence case. Since the latter has been studied in some detail by Shen *et al.* (1999), the decay of surface ω_z in the wake will not be taken up here.

Next we use the ω_z signature to investigate the wake meandering in DNS results. Figure 24 plots the time evolution of surface ω_z contours. As pointed out earlier, initially we input a small-magnitude unstable mode obtained from the OS analysis. As time increases, a meandering pattern forms. Compared to the experiment (figure 6), the amplitude of the meandering is relatively small here since the meandering is still developing. Nevertheless the meandering pattern is clear at late stages of the simulation.

The meandering of the wake is also demonstrated by the ω_z contours below the free surface, which are plotted in figure 7(ii). On departing from the free surface,

the meandering amplitude is found to decrease first and then increase. This is in agreement with the experimental result plotted in figure 7(i).

In a way similar to the experimental study, we quantify the meandering amplitude based on ω_z with the definition (3.4). The results are plotted in figure 9(b). The development of meandering is shown clearly by the increasing of A_m with time. Consistent with figures 6, 7 and 24, the meandering amplitude in the DNS is smaller than the experimental value shown in figure 9(a). Vertically, we find that the meandering amplitude is largest at the free surface. Away from the surface, A_m decreases first, reaching a local minimum at $z = -0.15 \sim -0.12$, and then increases. This variation is in agreement with the sparse data obtained by experiment (figure 9a). (A similar comparison of the meandering length L_m (cf. figure 8) can, in principle, also be made. In this case, however, with streamwise-periodic computational boundaries, such correlations are dominated by the computational domain length, and the comparison is not as meaningful.)

Finally, we show the effects of hull geometry on the meandering. Figure 10(ii) plots the surface signature of ω_z obtained from the DNS of the shallow hull (hull I) wake and the deep hull (hull III) wake. They both resemble well the experimental results shown in figure 10(i). Compared with the DNS result of hull II (figure 24), it is found that hull III has more intensive meandering while the meandering in hull I is less obvious. This is in agreement with the experimental study (figure 10i) and the OS analysis (figure 13). We remark that the meandering amplitude is the major effect of the beam-to-draught ratio. Other statistical and structural properties of the wakes of hulls I and III have been extensively examined. They possess the same characteristics as the hull II case detailed in the present paper and will not be taken up here.

6. Conclusions

We have performed a coordinated experimental, theoretical and numerical study of the turbulent wake flow behind towed ship models. In the experiment we use DPIV to obtain instantaneous whole-field measurements at multiple horizontal and vertical planes. In the theoretical study, we perform an Orr–Sommerfeld stability analysis for the mean wake profile using free-surface boundary conditions. Finally, we perform direct numerical simulations of the Navier–Stokes equations using the DPIV and OS data to construct the initial condition. To allow direct quantitative comparisons, the DPIV, OS and DNS are performed at the same Reynolds and Froude numbers corresponding to the experimental conditions. Good to excellent comparisons are obtained.

The most significant feature of wake flow is shown to be a meandering structure with well-defined (longitudinal) wavelength and (lateral) amplitude. The former satisfies a Strouhal scaling with respect to model beam and forward speed, while the latter is found to depend on downstream distance (or 'age') of the wake (and the depth). The DPIV quantification of these agrees well with OS predictions and DNS results. These latter analyses provide the mechanism and confirmation for the development of meandering features.

From the whole-field statistics, we quantify the highly anisotropic nature of the turbulent wake. Among the velocity components, the streamwise fluctuation dominates with maxima located at the free surface and offset from the centre-plane. Compared to the velocity, the vorticity field is less anisotropic except within a thin surface layer wherein the horizontal vorticity components diminish rapidly while vertical vorticity connects and becomes persistent. We also obtain spatial distributions of the velocity

and vorticity length scales, which show the effects of the vertical/horizontal stretching respectively of the vertical/horizontal vorticities near the surface.

To understand the effects of hull geometry, we consider three hulls with different beam-to-draught ratios. For a given beam, the meandering amplitude is shown to increase as the draught increases. This result can be anticipated from the Orr–Sommerfeld instability of the mean wake.

We remark that the present study is for small model scales at relatively low Reynolds and Froude numbers. This allows us to perform and obtain direct comparisons among the DPIV, DNS and OS. Under these conditions, the meandering of the wake caused by the instability of the wake shear flow is a predominant feature. For real ship wakes with much higher Reynolds numbers, the wake flow will be significantly more turbulent – the same instability mechanism is still expected (as supported by OS) but the manifestation of the meandering might be obscured by (other) turbulent processes. Our main objective here is a mechanistic investigation, which serves as a first step towards future study at larger scales. The Orr–Sommerfeld solver developed in this paper can be readily applied to high Reynolds and Froude numbers. Experimental extensions to higher Reynolds/Froude numbers are being pursued by a number of research groups (e.g. Dong, Katz & Huang 1997). Extension of the DNS to more realistic scales using large-eddy simulation with specialized free-surface subgrid-scale models (cf. Shen & Yue 2001) is now underway.

This research was financially supported by the Office of Naval Research.

REFERENCES

Adrian, R. J. 1991 Particle-imaging techniques for experimental fluid mechanics. *Annu. Rev. Fluid Mech.* **23**, 261–304.

Borue, V., Orszag, S. A. & Staroselsky, I. 1995 Interaction of surface waves with turbulence: direct numerical simulations of turbulent open-channel flow. *J. Fluid Mech.* **286**, 1–23.

Comte-Bellot, G. & Corrsin, S. 1971 Simple Eulerian time correlation of full- and narrow-band velocity signals in grid-generated, 'isotropic' turbulence. *J. Fluid Mech.* **48**, 273–336.

Dong, R. R., Katz, J. & Huang, T. T. 1997 On the structure of bow waves on a ship model. *J. Fluid Mech.* **346**, 77–115.

Gharib, M., Dabiri, D. & Zhang, X. 1994 Interaction of small scale turbulence with a free surface. In *Free-Surface Turbulence* (ed. E. P. Rood & J. Katz), pp. 97–102.

Handler, R. A., Swean, T. F. Jr, Leighton, R. I. & Swearingen, J. D. 1993 Length scales and the energy balance for turbulence near a free surface. *AIAA J.* **31**, 1998–2007.

Komori, S., Nagaosa, N., Murakami, Y., Chiba, S., Ishii, K. & Kuwahara, K. 1993 Direct numerical simulation of three-dimensional open-channel flow with zero-shear gas–liquid interface. *Phys. Fluids* A **5**, 115–125.

Kwak, D., Reynolds, W. C. & Ferziger, J. H. 1975 Three dimensional time dependent computation of turbulent flows. *Mech. Engng Dept., Stanford Univ. Rep.* TF-5.

Lam, K. & Banerjee, S. 1988 Investigation of turbulent flow bounded by a wall and a free surface. *Fundamentals of Gas–Liquid Flows* (ed. E. Michaelides & M. P. Sharma), pp. 29–38.

Munk, W. H., Scully-Power, P. & Zachariasen, F. 1987 Ships from space. *Proc. R. Soc. Lond.* A **412**, 231–254.

Perot, B. & Moin, P. 1995 Shear-free turbulent boundary layers. Part 1. Physical insights into near-wall turbulence. *J. Fluid Mech.* **295**, 199–227.

Sarpkaya, T. 1996 Vorticity, free surface, and surfactants. *Annu. Rev. Fluid Mech.* **28**, 83–128.

Shen, L., Triantafyllou, G. S. & Yue, D. K. P. 2000 Turbulent diffusion near a free surface. *J. Fluid Mech.* **407**, 145–166.

Shen, L. & Yue, D. K. P. 2001 Large-eddy simulation of free-surface turbulence. *J. Fluid Mech.* **440**, 75–116.

Shen, L., Zhang, X., Yue, D. K. P. & Triantafyllou, G. S. 1999 The surface layer for free-surface turbulent flows. *J. Fluid Mech.* **386**, 167–212.

Triantafyllou, G. S. & Dimas, A. A. 1989 Interaction of two-dimensional separated flows with a free surface at low Froude numbers. *Phys. Fluids* A **1**, 1813–1821.

Walker, D. T., Leighton, R. I. & Garza-Rios, L. O. 1996 Shear-free turbulence near a flat free surface. *J. Fluid Mech.* **320**, 19–51.

Zhang, C. 1996 Turbulent free-surface wakes behind towed model – experimental measurements, numerical simulations and stability analysis. PhD thesis, Department of Ocean Engineering, MIT.